

1 **Clonal evolution during metastatic spread in high-risk neuroblastoma**

2 Gunes Gundem^{1,2,†}, Max F. Levine^{1,2}, Stephen S. Roberts¹, Irene Y Cheung¹, Juan S. Medina-
3 Martínez^{1,2}, Yi Feng¹, Juan E. Arango-Ossa^{1,2}, Loic Chadoutaud², Mathieu Rita², Georgios Asimomitis²,
4 Joe Zhou^{1,2}, Daoqi You¹, Nancy Bouvier¹, Barbara Spitzer¹, David B. Solit^{3,4}, Filemon Dela Cruz¹,
5 Michael P. LaQuaglia¹, Brian H. Kushner¹, Shakeel Modak¹, Neerav Shukla¹, Christine A. Iacobuzio-
6 Donahue^{5,6,7}, Andrew L. Kung¹, Nai-Kong V. Cheung^{1*} and Elli Papaemmanuil^{1,2,†,*}

7

8 ¹Department of Pediatrics, Memorial Sloan Kettering Cancer Center, New York, NY, USA.

9 ²Computational Oncology Service, Department of Epidemiology & Biostatistics, Memorial Sloan
10 Kettering Cancer Center, New York, NY, USA.

11 ³Department of Medicine, Memorial Sloan Kettering Cancer Center, New York, NY, USA

12 ⁴Marie-Josée and Henry R. Kravis Center for Molecular Oncology, New York, NY, USA

13 ⁵The David M. Rubenstein Center for Pancreatic Cancer Research, Sloan Kettering Institute,
14 Memorial Sloan Kettering Cancer Center, New York, NY, USA

15 ⁶Human Oncology and Pathogenesis Program, Sloan Kettering Institute, Memorial Sloan Kettering
16 Cancer Center, New York, NY, USA

17 ⁷Department of Pathology, Memorial Sloan Kettering Cancer Center, New York, NY, USA

18

19 *Co-last authors

20 †Corresponding author

21

22 **Address for correspondence:** papaemme@mskcc.org; gundem@mskcc.org

23

24

25

26

27

28

29

30

31

32

33 **Abstract (100)**

34 High-risk neuroblastoma is generally metastatic and often lethal. Using genomic profiling of 470
35 sequential and spatially separated samples from 283 patients, we characterize subtype-specific
36 genetic evolutionary trajectories from diagnosis, through progression and end-stage metastatic
37 disease. Clonal tracing timed disease initiation to embryogenesis. Continuous acquisition of
38 structural variants at disease defining loci (*MYCN*, *TERT*, *MDM2-CDK4*) followed by convergent
39 evolution of mutations targeting shared pathways emerged as the predominant feature of
40 progression. At diagnosis metastatic clones were already established at distant sites where they
41 could stay dormant, only to cause relapses years later and spread via metastasis-to-metastasis and
42 polyclonal seeding after therapy.

43

44

45

46

47

48

49

50

51

52

53

54

55

56

57

58 **Introduction**

59 Neuroblastoma is an embryonal tumor arising from the developing sympathetic nervous system
60 accounting for 15% of pediatric cancer mortality¹. Disease presentation is highly heterogeneous and
61 ranges from low-risk local-regional tumors to widely disseminated high-risk disease seen in two
62 thirds of the patients. For high-risk neuroblastoma (HR-NB), modern clinical management includes
63 multimodal chemotherapy, surgical resection, radiotherapy and immunotherapy. Nevertheless,
64 despite intensive treatment 50% of HR-NB patients still relapse with fatal outcomes².

65

66 Notwithstanding the metastatic nature of HR-NB, most genomic studies of disease progression
67 focused on small cohorts of paired diagnostic-relapse tumors³⁻⁹. Recently, broad copy number
68 aberrations (CNA) and whole-exome sequencing (WES) from multi-region biopsies suggested
69 elevated genetic heterogeneity in high-risk disease¹⁰⁻¹². However, the majority of disease-defining
70 alterations in HR-NB^{13,14} result from structural variants (SVs) that cannot be captured by low-
71 resolution WES/CNA analysis. To date, the temporal and spatial genomic features of disease
72 progression as patients go through multiple lines of therapy are not well understood. Here, we
73 leverage the MSKCC neuroblastoma biobank to study a unique cohort of 470 tumors from 283
74 patients representative of HR-NB at diagnosis, consecutive relapses, and diverse metastatic sites.
75 Using a combination of whole genome (WGS) and targeted sequencing approaches we characterized
76 the composite genetic alterations associated with neuroblastoma pathogenesis and define the
77 lineage relationships during disease progression across diverse neuroblastoma molecular subtypes.

78

79 **Results**

80 **Cohort ascertainment**

81 Our cohort consisted of 470 tumors from 283 patients with predominantly stage-4 disease (87%)
82 and/or spatially and temporally separate tumors available (Fig. 1a and Supplementary Table 1).

83 Fresh-frozen surgical specimens were collected at consecutive clinical intervention time points
84 including: 110 pre-treatment diagnostic samples, 5 therapy-naive re-resections, 132 therapy
85 resection during induction chemotherapy (t-resection), 111 relapses and 112 further relapses (1-17
86 samples per patient) and spanned spatially separated disease sites including: 217 samples from
87 primary site, 150 from local-regional spread and 97 from metastases as defined by clinical
88 guidelines¹⁵ including rare metastatic sites such brain. A web portal describing the treatment
89 timelines and clonal phylogenies for patients with two or more tumors is provided in
90 (<https://master.d32nckcows37aj.amplifyapp.com/>) and detailed summaries of genomic and clonal
91 evolution patterns in 45 patients with multi-WGS data are provided in Supplementary Information.

92

93 **Landscape of genomic alterations**

94 Comprehensive genomic profiling (substitutions, indels, SVs and CNAs) (Extended Data Fig. 1a-b,
95 Supplementary Table 2) identified both established and novel gene mutations linked to
96 neuroblastoma pathogenesis. The genomic landscape was representative of HR-NB^{16,13,17}. Only 4
97 genes (*MYCN*, *ALK*, *TERT*, *ATRX*) had mutations in >10% of patients while recurrent *MDM2-CDK4* co-
98 amplification was observed in 3%¹⁸. Alterations in *MYCN*, *TERT*, *ATRX* and *MDM2-CDK4* defined
99 mostly non-overlapping disease subtypes explaining 51% of the cohort while *ALK* mutations were
100 shared across the cohort. 41% and 8% of the patients did not have any subtype-defining alterations
101 other than segmental (SEG-CNA) or numeric chromosome-level CNAs (NUM-CNA), respectively.

102

103 *TERT* rearrangements are common in neuroblastoma^{13,14}. Here, we report *TERT*_p substitutions in 9
104 patients comprising 17% of the *TERT* events. However, contrary to *TERT* SVs which are mutually
105 exclusive to other subtype defining events, *TERT*_p mutations were enriched in *MYCN*-amplified
106 (*MYCN-A*) neuroblastoma and demarcated a group of *MYCN-A* patients with a trend for rapid
107 progression and death within 2 years from diagnosis (Extended Data Fig. 1c). PI3K-mTOR pathway

108 was also mutated in 5% of the patients suggesting enrichment in HR-NB compared to primary
109 neuroblastoma (<1% in Brady et al¹⁴). Additionally, mutations in neuroblastoma differentiation
110 genes including *RARA*, *RARB*, *PHOX2B*, *SPRY2*, *IGF2BP3* and *WNT5A* were observed in 4% of the
111 patients at relapse (Supplementary Information).

112

113 **Evolution of mutational landscape in response to therapy**

114 Analysis of genome-wide mutation landscapes revealed distinct mutational patterns at diagnosis and
115 relapse (Extended Data Fig. 2a-b and Supplementary Table 1). At diagnosis, two substitution
116 signatures, SBS40 and SBS18, were differentially enriched across molecular subtypes. Mutations
117 attributed to SBS40, similar to the clock-like signature SBS5¹⁹, was higher in *ATRX*-mutated patients
118 and correlated with age at diagnosis, while SBS18, which is predominantly defined by C>A mutations,
119 prevailed in *MYCN-A* tumors in agreement with prior literature¹⁴ and did not correlate with age (Fig.
120 1b and Extended Data Fig. 3a). SBS18 was first described in neuroblastoma²⁰ and attributed to
121 reactive oxygen species (ROS)²¹. *MYCN-A* enhances glutaminolysis in neural crest progenitor cells,
122 which in turn induces oxidative stress by ROS production²². Expression of glutaminolysis signature
123 was higher in *MYCN-A* tumors compared to other subtypes (Extended Data Fig. 3b). This provides a
124 plausible mechanistic link between *MYCN-A*, metabolic reprogramming and SBS18 burden. Notably,
125 the glutaminolysis gene expression signature and the rate of accumulation of SBS18 remained stable
126 during disease progression (Extended Data Fig. 3b).

127

128 Pediatric tumors are defined by low tumor mutation burden (TMB)²³. TMB was low at diagnosis^{24,23}
129 (median=0.52 muts/Mb, range=0.06-2.6) (Fig. 1c) but increased significantly during disease
130 progression (median=2.2 muts/Mb, range=0.2-9). Notably, in patients with matched
131 diagnostic/relapse tumors, TMB increased by 6- and 14-fold at first and later relapses (Fig. 1d),
132 respectively, approximating TMB ranges seen in adult tumors²⁰. At diagnosis neuroblastoma is

133 characterized by an immune-cold tumor microenvironment²⁵⁻²⁷ (TME) with poor responses to
134 immune checkpoint blockade therapy^{28,29}. We evaluated whether the increased TMB during disease
135 progression presented a therapeutic opportunity mediated by putative neo-antigens³⁰. However,
136 despite the increase in predicted neoantigen burden, there was no association with transcriptional
137 patterns suggestive of an immunomodulatory switch during disease progression (Extended Data Fig.
138 3c).

139
140 At relapse, increase in TMB was associated with exposure to chemotherapy-associated mutation
141 signatures³¹. Specifically, three substitution signatures (TMZ, SBS31 and SBS35) dominated by T>C
142 and C>T mutations correlated with exposure to temozolomide and platinum with evidence of strong
143 dose-response relationships^{32,21,31,19} (Fig. 1e-f). At disease progression, tumors from prior radiated
144 sites had an excess of small deletions, SV deletions, reciprocal translocations and complex events^{33,34}
145 (Supplementary Fig. 1). This demonstrates that therapy directly molds the mutation landscape of
146 HR-NB tumors. Thus, we next evaluated the effect of these mutation processes in the driver
147 landscape at diagnosis and during disease progression. Of 82 oncogenic substitutions from WGS data,
148 48 were present at diagnosis and 34 emerged at relapse. Notably, only 12% of the oncogenic
149 substitutions were assigned to a therapy-related signature compared to all relapse-specific SNVs
150 (34%) (Extended Data Fig. 3d).

151
152 **Timing the emergence of the initial neuroblastoma clone**
153 For each patient, clonal reconstruction of tumor phylogenies delineated the trunk marked by the
154 mutations found in 100% of malignant cells in all tumors of a patient as well as subclonal events (not
155 on trunk). Trunk represents the most recent common ancestor (MRCA) (Online Methods and
156 Supplementary Information, Supplementary Fig. 2-46 and Supplementary Tables 3-4). The number
157 of clock-like mutations on the trunk can be used to estimate the time of MRCA emergence³⁵⁻³⁷. Across

158 39 evaluable patients the number of truncal substitutions (trunk length) was low (median=753,
159 range=11-5801) and correlated with age at diagnosis only when disease subtype, stage, and number
160 of tumors were taken into account (Fig. 2a and Supplementary Fig. 47). Low-stage disease tended to
161 have shorter trunks (Fig. 2b) with lengths comparable to the number of substitutions detected in
162 non-malignant clones in bulk placenta also enriched for SBS18 mutations³⁸. This suggests that the
163 first malignant clone emerges in similar time frames during embryogenesis. Indeed, chronological
164 timing of MRCA emergence using the clock-like SBS40 mutations³⁷ confidently pinpointed an
165 embryonic and post-natal origin in 6 and 8 cases, respectively. For the remaining 25 patients the
166 confidence intervals were large, owing to low numbers of mutations on the trunk (Fig. 2c). Notably,
167 MYCN-A was common in embryonic origin (4/6) while ATRX-mutant disease was enriched for post-
168 natal onset (7/8) especially in patients with *ATRX* truncating mutations (Fig. 2c).

169

170 **Subtype-specific evolutionary trajectories underwrite disease progression**

171 Analyses of multiple samples representative of the clinical course of treatment from 94 patients
172 across HR-NB subgroups identified previously unappreciated and subtype-specific evolutionary
173 trajectories for tumors with *MYCN-A*, *TERT-SV*, *ATRX* events and *MDM2-CDK4* co-amplification (Fig.
174 2d-e, Extended Data Fig. 4-5 and Supplementary Data fig. 2-46 and 48-53). While subclonal events at
175 RAS-MAPK^{4,5,39} and PI3K-mTOR pathways were common across subtypes, the acquisition of SVs
176 emerged as critical events in disease evolution with a striking propensity to repeatedly target the
177 main subtype-defining driver genes *MYCN*, *TERT* and *ATRX* (Fig. 2d-e).

178

179 Tumor-initiating *MYCN* amplifications in neuroblastoma⁴⁰ are frequently found in extrachromosomal
180 DNA^{41,42}, which may result from simple or complex SVs at the trunk of the tumor phylogeny. Amongst
181 patients with multi-WGS data, we observe continuous rearrangements of the *MYCN* locus in both
182 primary (7/10 cases) and relapse sites (9/11 patients) (Fig. 2e, Fig. 3a and Supplementary Fig. 54-

183 56). During therapy, rearrangements at the *MYCN* locus continued to accumulate in 9/10 patients
184 and in four of these patients a clone with chromothripsis at the *MYCN* locus dominated across
185 metastatic sites without evidence of further diversification (Supplementary Fig. 54-56).

186
187 *TERT*-SVs are mutually exclusive with *MYCN* and *ATRX* rearrangements, thus demarcate a distinct
188 HR-NB subtype^{13,17}. In our cohort *TERT*-SVs were enriched in CNS metastases (8/19 patients)⁴³.
189 Intriguingly, unlike *MYCN*, where an initial amplification is always present on the trunk, *TERT*-SVs
190 were predominantly (10/13 SVs) subclonal to segmental CNAs (Fig. 2d-e, Fig. 3b and Extended Data
191 Fig. 5). Similar to the *MYCN* locus, we observe continuous *TERT* rearrangements in the majority of
192 cases (5/7) during disease progression. These relapse-specific rearrangements result in increased
193 copy number and expression of *TERT* consistent with an increasing addiction to *TERT* signaling (Fig.
194 3b, Extended Data Fig. 5 and Supplementary Fig. 3, 5, 18-20 and 24-25).

195
196 *ATRX*-mutant neuroblastoma is seen in older patients with indolent disease^{44,45}. In contrast to *MYCN*-
197 A and *TERT*-SV patients who were stage-4 at diagnosis, 21% of *ATRX*-mutant cases were diagnosed
198 with low-stage disease but eventually relapsed. Subclonal acquisition of *ATRX* events were common
199 (9/29 events) and seen in relapses (Extended Data Fig. 4). In two patients, parallel acquisition of
200 *ATRX* mutations were seen at distinct metastatic sites (H135089) or locoregional relapses at
201 consecutive time points (H134817) (Fig. 3c). *ATRX*-mutant cases were also enriched for SVs affecting
202 *PTPRD* (Extended Data Fig. 1e) with evidence of parallel or continuous evolution (Fig. 3c and
203 Extended Data Fig. 4).

204
205 *MDM2-CDK4* co-amplifications were seen in patients diagnosed with low-stage disease
206 (Supplementary Table 1). Notably, the co-amplification was not mutually exclusive with *ATRX* events
207 and *TERT*-SVs suggesting an overlapping subtype (Fig. 2d-e). For example, phylogenetic

208 reconstruction for patient H132384 mapped truncal *MDM2-CDK4* co-amplification and subclonal SVs
209 at *ATRX* and *TERT*. However, the *ATRX* and *TERT* events were acquired on two distinct subclonal
210 lineages further validating the mutually exclusivity of these events (Fig. 3b). In patients with *MDM2-*
211 *CDK4*, subclonal *ATRX* events and continuous evolution at *MDM2-CDK4* locus via incorporation and
212 over-expression of other genomic loci (*TERT*, *WNT3A*, *IGF2BP3*) were seen during disease
213 progression (Extended Data Fig. 4), which might contribute to the dismal outcomes associated with
214 *MDM2-CDK4*¹⁸.

215
216 *TP53* mutations demarcate an ultra HR-NB subtype^{46,47}. Excluding arm-level CNAs at 17p (n=19, 7%),
217 10 patients had mutations (n=10) or SVs (n=4) at the *TP53* locus specifically. In 7/10 patients these
218 mutations were bi-allelic, most frequently by initial 17p loss followed by a *TP53* mutation (n=5).
219 Parallel acquisition of mutations affecting p53 pathway were observed both within the primary site
220 (H116987) and in different metastatic tumors (H134722) (Fig. 3d).

221
222 Taken together this analysis demonstrate that in neuroblastoma subtype-specific evolutionary
223 trajectories are predominantly determined by SVs targeting the main driver gene itself with specific
224 acquisition of secondary hits (e.g. *TERT*_p in *MYCN-A* and *PTPRD* in *ATRX*-mutant) and are followed
225 by subclonal mutations in RAS-MAPK, PI3K-mTOR and p53 pathways shared across the disease
226 subtypes.

227
228 **Clonal diversification at primary site creates multiple clones with metastatic potential**

229 Patients with HR-NB are diagnosed with widely metastatic disease (bone, bone marrow, liver, lung
230 and CNS)⁴⁸. We studied the clonal relationships amongst primary and disseminated disease in 30
231 evaluable patients (Methods, Supplementary Tables 3-5).

232

233 Whilst all resections were clonally related, subclonal heterogeneity at the primary site was seen in
234 the majority of patients in the form of subclonal CNAs and oncogenic mutations/SVs (83%, 25/30)
235 (CCF median=100%, range=4-100%) (Extended Data Fig. 4-5). This subclonal diversification in the
236 primary site creates distinct cell subpopulations with differential capacity to spread. Analysis of the
237 ensuing metastatic trajectories demonstrates that distinct primary-metastasis pairs share closer
238 lineage relationships in the tumor phylogeny than the primary sites to one another (7/9 patients,
239 Extended Data Fig. 4-5). For example, in patient H103207 (Fig. 3a), clonal structure across two
240 adrenal tumors at diagnosis and 6 metastases from CNS, lungs and liver suggests that CNS-metastatic
241 clone separated from the trunk before the adrenal primary site diversified further. Similarly, one of
242 the two adrenal tumors segregated with the lineage leading to liver and lung metastases. This
243 demonstrates that branching evolution in the primary site gives rise to multiple subclones with the
244 potential to spread. This observation held true across disease subtypes of this cohort (Extended Data
245 Fig. 4-5 and Supplementary Table 3).

246

247 **Timing of metastasis with respect to therapy**

248 Detection of therapy-related mutation signatures indicates the presence of cells that survived
249 therapy and subsequently achieved a clonal representation detectable at WGS depth. Therefore,
250 mutational signatures can be used to time emergence of clones relative to the time of therapy⁵⁰. We
251 illustrate this point with patient H118706 (5-yo, *MYCN-A*, stage-4) for whom WGS was performed on
252 two diagnostic tumors (adrenal and liver metastasis) and 15 metastatic sites including liver and lungs
253 at autopsy following unsuccessful treatment with platinum and temozolomide (Fig. 4a). Subclonal
254 structure suggests that all the autopsy tumors came from the same *TP53*-mutant clone with strong
255 exposure to platinum signatures (48% of the substitutions) and this clone was succeeded by six
256 clones with evidence of temozolomide signature (5-19%). This suggests that the *TP53*-mutant clone

257 emerged after platinum therapy and seeded all the metastatic tumors from autopsy when
258 temozolomide therapy started.

259

260 Using the same logic, in 13 evaluable patients we studied the relative timing of the emergence of 21
261 metastasizing subclones and 26 daughter subclones (Supplementary Tables 3-4, Extended Data Fig.
262 6 and Supplementary Information). Majority of the metastasizing subclones (18/21) had no
263 evidence of therapy exposure, suggesting that disease dissemination happens before therapy
264 consistent with widely metastatic presentation at diagnosis (Extended Data Fig. 6). Importantly, this
265 observation held true not just for local spread but across distant sites including CNS metastases (3/4
266 patients), which are typically not detected by imaging at diagnosis⁵¹. Notably, exposure to therapy-
267 related mutational signatures was seen in most (22/26) daughter subclones that emerge from the
268 initial metastasizing subclone (CCF median=80%, range=15-100%) in line with on-therapy disease
269 progression at the metastatic sites.

270

271 **Origin of late relapses traced back to early clones followed by a long period of dormancy**

272 With improved treatment and prolonged survival, consecutive relapses are increasingly observed
273 amongst HR-NB patients. For 72 patients in our cohort, we were able to study 114 clonal transitions
274 from primary to first relapse (47 patients) and/or between consecutive relapses (43 patients). We
275 observed three distinct patterns of temporal transitions (Supplementary Tables 3 and 6 and Fig. 4b-
276 c). Majority of the relapses were accompanied by accumulation of additional CNAs or mutations/SVs
277 at recurrent loci (72%) (linear and branched in Fig. 4b-c). In 24%, relapses were seeded by exactly
278 the same clone without evidence of new genetic changes and in 4% by an earlier clone in the
279 phylogeny. All three patterns were equally common from diagnosis to first relapse, amongst
280 consecutive relapses as well as across disease subtypes (Fig. 4b). This suggests that while subclones
281 with new drivers continue to emerge and replace existing ones, biological themes are preserved. In

282 31/45 patients with clonal transitions happening as a switch between different branches, the same
283 pathway was exploited by the tumor consistent with pathway-specific dependencies (Fig. 4c).

284

285 For patients with three or more consecutive relapses, we were able to capture multiple waves of
286 clonal successions and transitions across years. For example, for H134819 (3.5-yo stage-I *MYCN*-NA)
287 the same relapsing clone with a *SPRY2* deletion⁵² and a high-level amplification of *IGF2BP3* via *MDM2*-
288 *CDK4* SVs was present across all five locoregional recurrences from 2.7 to 3.4 years after diagnosis,
289 with late clonal switches from an *ALK* to a *PIK3R1*-mutant subclone and finally to a subclone with
290 *ATRX* and *CDKN1C* events (Fig. 4d). By contrast, in the case of H134821 (9-yo stage-I *MYCN*-NA), the
291 first two locoregional relapses within 4-6 months from diagnosis were caused by a *PIK3CA*-mutant
292 subclone while the last two relapses 8 years later hailed from an *MTOR*-mutant clone (Fig. 4e). Both
293 of these relapsing clones were present at diagnosis suggesting that subclones can stay dormant for
294 many years, remain clinically undetectable but nonetheless maintain the potential to instigate
295 relapses at much later time points. These findings suggest that chemo-resistant clones with specific
296 driver mutations may already exist at diagnosis and, in rare cases, can lay dormant for years before
297 gaining clonal dominance as patients go through multiple lines of therapy.

298

299 **Shared lineage relationship across locoregional and distant metastases**

300 We next studied the relationships between locoregional disease and distant metastasis by evaluating
301 data from 19 patients with 69 tumors from disseminated sites (Methods, Supplementary Table 3).
302 We observe an equal number of relapsing subclones involved in locoregional extension or distant
303 metastasis (average 1.5 vs 1.3 subclones) suggesting that there is no differential propensity to extend
304 locally or metastasize. In support of this notion, the same clone from the primary site seeded both
305 locoregionally and at metastatic sites in the four patients with available tumors (30 samples)
306 (Extended Data Fig. 4-5).

307

308 **Polyclonal and metastasis-to-metastasis seeding after therapy**

309 Despite high intensity multimodal therapy, 50% of HR-NB patients will eventually progress, typically
310 in metastatic sites. To compare the clonal representation across distant metastatic sites, we studied
311 10 patients with two or more metastases (Supplementary Table 4). In most cases the same subclone
312 seeded all metastatic tumors (5/7 patients) (Fig. 4a, Fig. 5, Extended Data Fig. 4-5 and Supplementary
313 Information). This occurred in the form of polyclonal seeding⁵³ during or after therapy, as evidenced
314 by the presence of therapy related mutation signatures in the metastatic clones (e.g H103207,
315 H118706 and H134722) (Supplementary Information).

316

317 We also see unequivocal evidence of metastasis-to-metastasis (met-to-met) seeding. Patient
318 H118706 was diagnosed with metastatic disease in both the lungs and liver. Interestingly, analysis
319 from 16 tumors from the same metastatic sites 16 months later at autopsy demonstrated that all sites
320 were seeded by the same therapy-exposed subclone originating from the liver metastasis (Fig. 4a).
321 This suggests that the metastatic clones in lungs and liver at diagnosis were cleared by chemotherapy
322 yet a therapy-resistant subclone escaped from the liver and successfully re-seeded multiple
323 metastatic deposits across the same anatomical sites.

324

325 Notably the subclones shared across metastases were often characterized by oncogenic events such
326 as the hyper-rearranged *MYCN-A*, convergent *TP53* mutations and *ALK* mutations. This suggests that
327 certain therapy-resistant subclones with selective advantage⁵⁴ have the capacity to disseminate and
328 successfully establish clinically detectable metastatic lesions that transverse locoregional sites, lung,
329 and liver and CNS.

330

331

332 **Discussion**

333 Our understanding of the temporal and spatial relationships underlying evolution of neuroblastoma
334 from disease initiation through treatment, progression and metastasis has remained obscure.
335 Leveraging surgical samples from a unique cohort of 283 patients, we performed a comprehensive
336 analysis of genomic evolution throughout the natural course of the disease.

337

338 Clonal reconstruction using multi-sample WGS data traced the first malignant clone and the ensuing
339 subclonal trajectories with notable differences amongst different molecular subtypes. We estimate
340 that *MYCN*-A emerges during embryogenesis while *ATRX*-mutant disease is frequently post-natal.
341 Unlike *MYCN*, which is always targeted on the trunk, *TERT* and *ATRX* events are not always found in
342 the first malignant clone suggesting that they may not be required for disease initiation but yet, as
343 secondary events, define distinct and non-overlapping clinical subtypes with unique evolutionary
344 trajectories. Once established, tumors progress across time and space via a process underwritten by
345 continuous or parallel acquisition of SVs at disease-defining loci namely *MYCN*, *TERT*, *ATRX* and
346 *MDM2-CDK4*. Whilst it is likely that high-level amplifications create genomic instability thereby
347 providing fuel for continued rearrangements, subclonal events at these loci might provide survival
348 advantage under chemotherapeutic pressure, only to become stable at their most complex forms
349 shared across multiple metastatic sites as evidenced by the dominance of clones with the same
350 complex but stable *MYCN* amplicon in late stage metastatic disease. Although this is in agreement
351 with the emerging importance of evolution through extrachromosomal DNA observed in
352 neuroblastoma and other tumor types^{56,57}, study of larger sample sets is warranted to further validate
353 these observations.

354

355 Analysis of temporally and spatially separated tumors revealed unique patterns and timing of disease
356 spread. At diagnosis, primary disease is already carrying divergent subclones with parallel drivers

357 involved in multiple waves of metastatic spread early in disease evolution. This is in agreement with
358 the idea that clonal heterogeneity is established early in neuroblastoma pathogenesis. As the disease
359 progresses, patients go through multiple lines of therapy, with each consecutive relapse
360 underwritten by the emergence of subclones with new driver mutations affecting the same set of
361 pathways. Furthermore, we show that most metastases occur prior to the commencement of therapy,
362 consistent with the clinical presentation of HR-NB. This is particularly true for CNS metastases which
363 have a low incidence⁵¹ and are rarely detected clinically at diagnosis⁵¹. This suggests that CNS
364 involvement becomes detectable only after systemic disease was debulked and controlled by drugs
365 that did not cross the blood brain barrier.

366
367 Curative treatment for neuroblastoma is aimed at killing invisible metastases. Indeed we
368 demonstrated that disseminated disease could remain dormant for a long period (up to 10 years)
369 after successful treatment, whilst the patient is clinically “disease-free”, but then eventually relapse
370 and spread to new sites. Despite the observed heterogeneity at the primary site, we show that late
371 metastatic spread after therapy is underwritten by a set of subclones that can spread across
372 locoregional and distant metastatic sites via met-to-met and polyclonal seeding. This suggests that
373 therapy selects for particularly resistant and aggressive subclones with superior metastatic potential.

374
375 Taken together our data built a dismal picture of neuroblastoma pathogenesis, where malignant
376 clones arise early in embryogenesis, yet rapidly diversify and spread across local and distant
377 metastatic sites prior to disease diagnosis and unravel the complex networks of disease spread
378 during relapse in response to therapy. This dynamic and rapidly evolving disease presentation has
379 important implications for inclusion of select targeted agents in upfront therapy for HR-NB patients
380 in order to improve the chance of cure^{58,59}.

381

382 **Online methods**

383 **Patient cohort**

384 Patients in this cohort were seen in the Neuroblastoma clinic at the Memorial Sloan Kettering Cancer
385 Center (MSKCC) from 1987-2021. A written informed consent for tumor/normal sequencing and use
386 of clinical data was taken for all patients in accordance with the ethical rules and regulations of the
387 institutional review board at MSKCC. Additionally three patients' guardians consented to participate
388 in the MSKCC medical donation program.

389

390 **Chemotherapy regimen**

391 Detailed treatment information was available for 56 patients for whom 256 tumors were whole-
392 genome sequenced. Of these, 29 cases received induction chemotherapy as per an MSK protocol (N5,
393 N7, N8 or N9) in which the first five cycles consist of cyclophosphamide/doxorubicin/vincristine
394 (CAV) x 2, cisplatin/etoposide (PVP), CAV, PVP and CAV. 14 patients were treated according to a COG
395 regimen similar to ANBL0532 in which the first five cycles include cyclophosphamide/topotecan x 2,
396 PVP, CAV and PVP while 4 patients were treated according to COG3973 (CAV x 2, PVP, CAV and PVP).
397 The rest of the 8 patients were treated with other protocols containing 3-4 rounds of platinum-based
398 chemotherapy including 1 patient with rapid COJEC. Therapy resection (t-resection) tumors were
399 taken during induction chemotherapy after (3-5) cycles of chemotherapy. Of the 30 patients with
400 WGS data from a t-resection tumor, 21 tumors were exposed to only 1 round of platinum-based
401 chemotherapy while 8 and 1 were exposed to 2 and 3 rounds, respectively.

402

403 **Whole genome and transcriptome sequencing data**

404 WGS data for this study cohort came from three different sequencing centers. 1) 45 tumors and
405 matched normals were sequenced at St Judes Children Hospital at a median coverage of 34X for both
406 tumor and normal (range 30-59X)⁴⁴. Publicly available raw data for tumors and normals were

407 downloaded. 2) For 29 tumors and matched normals sequencing library preparation and WGS were
408 performed at the New York Genome Center as described before⁶⁰. Tumors and matched normals
409 were sequenced to a median of 95x (range 73-300X) and 44x (29-88X), respectively. 3) For 173
410 tumors and matched normals WGS was performed at a median coverage of 83X (40-181X) and 46X
411 (range 36-89X) at MSKCC as described in Supplementary Information. Within the subset of patients
412 where clonal structure was analyzed from multi-WGS data, genome-wide coverage figures were 50-
413 100X for 85% and >100X for 13% of the tumors. Only 6 tumors (all diagnostic) from 6 different
414 patients had <50X coverage. To supplant for lower coverage in the diagnostic tumor at least one
415 additional diagnostic tumor was sequenced whenever available (5/6 patients). RNA sequencing was
416 performed in-house as described in Supplementary Information to achieve a median of 81.5 million
417 paired reads per sample.

418

419 **Targeted gene panel sequencing**

420 DNA extracted from formalin fixed paraffin embedded (FFPE) tumor and blood samples (as a
421 matched normal) were sequenced using MSK-IMPACT, an FDA-approved and New York State
422 Department of Health validated panel used to sequence patients' tumors at MSKCC. MSK-IMPACT
423 captures protein-coding exons of 468 cancer-associated genes, introns of frequently rearranged
424 genes and genome-wide copy number probes⁶¹. Tumor samples were sequenced at a median depth
425 of 648X, whereas peripheral blood samples at 400x. Established pipelines followed by manual review
426 were used to characterize germline and acquired somatic mutations, copy number variants (CNVs)
427 and if targeted, genomic rearrangements as previously described⁶¹. Clinically relevant findings were
428 annotated using OncoKb tiers 1-4⁶².

429

430 **Bioinformatic analysis of WGS and RNA-seq**

431 Analysis of WGS and RNAseq data was executed using Isabl platform⁶³ and included: 1. Data quality
432 control; 2. Ensembl variant calling for germline and somatically acquired mutations from at least
433 two out of three algorithms run for each variant class and 3. Variant classification. Briefly, upon
434 completion of each sequencing run, Isabl imports paired tumor-normal FASTQ files, executes
435 alignment, quality control algorithms and generates tumor purity and ploidy estimates. For tumor
436 samples ensembl variant calling for each variant class (substitutions, insertions and deletions and
437 structural variations) was performed. High confidence somatic mutations are classified with regards
438 to their putative role in cancer pathogenesis and statistical post-processing enables the derivation of
439 microsatellite instability scores and mutation signatures²⁰. RNA-seq data were independently
440 analyzed for acquired fusions and gene expression metrics.

441 Clinical relevance of mutations in common cancer genes was annotated using OncoKb, COSMIC,
442 Ensembl Variant Effect Predictor, VAGrENT, gnomAD and ClinVar databases ^{62,64-67}.

443 Details of the variant calling and annotation can be found in the Supplementary Information.

444

445 **Gene expression analysis**

446 Gene expression for 55,390 coding and non-coding genes were ascertained in Transcripts Per Million
447 (TPM) using SALMON (v0.10.0, <https://github.com/COMBINE-lab/salmon>)⁶⁸. Genes with total
448 expression less than or equal to median across all genes were filtered. Deconvolution of the RNA-seq
449 data to predict the proportion of immune and stromal cells in the tumor microenvironment was done
450 using xCell⁷².

451

452 **Identification of mutation signatures for substitutions and indels**

453 De novo mutational signature analysis was performed using sigProfilerExtractor⁷³ with default
454 parameters. The signatures identified were compared to the COSMIC Mutational Signatures (v3.2)

455 with the addition of temozolomide signature from Kucab et al^{21,74} using cosine similarity. Details of
456 mutational signature analysis can be found in the Supplementary Information.

457

458 **Identification of simple and complex rearrangement events**

459 All structural variants called in a tumor were clustered into simple events (deletion, tandem
460 duplication, unbalanced translocation, balanced translocation, reciprocal inversion) or clustered
461 events (complex with ≥ 2 SVs) using ClusterSV [<https://github.com/cancerit/ClusterSV>]. The
462 algorithm groups the SVs into clusters based on the proximity of breakpoints, the number of events
463 in the region and the size distribution of those events. The resulting clusters contain SVs that are
464 significantly closer than expected given the orientation and the number of SVs in that tumor and
465 hence are expected to have happened as part of the same event. The resulting clusters were then
466 heuristically refined as described previously⁷⁵. Independently, SV breakpoints and CN data from
467 Battenberg and/or Brass were analyzed using ShatterSeek⁷⁶ to identify chromothripsis events.

468

469 **Inference of clonal structure from WGS data**

470 For 45 patients with 170 tumors for whom two or more WGS tumors were available, clonal structure
471 was determined using genome-wide substitutions, indels, SVs and CNAs separately. Within this
472 subset of WGS data, genome-wide coverage figures were 50-100X for 85% and $>100X$ for 13%. Only
473 6 diagnostic tumors from 6 different patients had $<50X$ coverage. For 5/6 of these patients at least 1
474 other tumor from diagnosis was sequenced to supplant for lower coverage (Supplementary
475 Information). Phylogenies predicted from substitutions and CNAs are displayed in the
476 Supplementary Figures 2-46.

477

478 For substitutions, union of high confidence mutations called across all tumors of the patient was used
479 as input to DPclust (v0.2.2, <https://github.com/Wedge-Oxford/dpclust>). Mutations were filtered if

480 they 1) had depth greater than 6 standard deviations above median coverage, 2) had no CN
481 information or 3) were in genomic regions that were affected by deletion or copy-neutral LOH in a
482 subset of the tumors of the patient. DPClust algorithm 1) calculates cancer cell fraction (CCF)
483 corrected for purity and local copy number 2) performs clustering across tumors to identify the CCF
484 position for the underlying clusters and 3) assigns mutations to each cluster^{77,53}. After heuristic and
485 manual curation of the clusters whenever needed, clusters that predominantly contain mutations
486 located on the chromosome were filtered. Clonal ordering of high-confidence clusters was
487 determined using clonevol (v0.99.11, <https://github.com/hdng/clonevol>)⁷⁸. When there are multiple
488 possible tumor phylogenies, clones with uncertainty were indicated with a star in the phylogenetic
489 tree. Mutational signatures were computed in each cluster independently. Signature trees were
490 generated with python matplotlib (v3.1.0, <https://matplotlib.org/>). All steps were run using an
491 inhouse wrapper.

492 For indels the same filtering criteria as substitutions was used with an additional filtering step prior
493 to clustering. Only indels across loci with tumor depth $\geq 40x$ and $\leq 200x$ and with a VAF of $>1\%$
494 were used.

495 In order to compare the CNA segments in a patient, first aberrant segments are matched to SV
496 breakpoints using the script called “match_rg_patterns_to_library.pl” from the Brass pipeline
497 [https://github.com/cancerit/BRASS/blob/dev/perl/bin/match_rg_patterns_to_library.pl]. The

498 presence of associated SVs across all the tumors (see the next section) is used to determine if CNA
499 breakpoints are shared or tumor-specific. Finally the results are manually cross-checked by

500 comparing the allele-specific and subclonal CN states for the segments as estimated by Battenberg.

501 In addition to this, a separate analysis was performed to construct phylogenies based on CNA
502 segments only using MEDICC2 with default parameters

503 [<https://bitbucket.org/schwarzlab/medicc2/src/master/>].

504

505 **Determining clonal status of SVs in a patient**

506 For all the SVs identified across the tumors of a patient, a pileup procedure was performed to
507 determine the number of aberrant reads supporting the variant in each tumor as described in
508 Supplementary Information. An SV was deemed 'present' in tumors with ≥ 2 reads supporting the
509 associated breakpoints. SV clusters were defined as groups of SVs present in the same set of tumors.

510

511 **Comparison of substitutions, indel and SV clusters**

512 Substitution and indel clusters were compared by calculating the cosine similarity of the CCF values
513 across all tumors of the patient. Clusters with a cosine similarity > 0.9 were matched. When a
514 substitution cluster matched multiple indel clusters, the pair with the smallest summed CCF
515 difference across the tumors was retained. Substitution and SV clusters were compared by their
516 presence across the different tumors of the patient. That is, an SNV cluster present in samples A, B
517 and C is matched with an SV cluster present in the same set of samples.

518

519 **Inference of clonal structure from targeted sequencing data**

520 For a subset of 49 patients with 113 tumors that were sequenced with MSK-IMPACT and/or WGS,
521 analysis of clonal structure was confined to the alterations that can be captured by MSK-IMPACT.
522 This includes the substitutions and indels called within the exonic and extended splice site regions
523 of ~ 450 cancer genes, focal deletions in genes such as *CDKN2A*, *PTPRD*, *ATRX* and *TP53*, structural
524 variants in select introns included in targeted sequencing panel in genes such as *ALK*, *ATRX* and *TP53*
525 as well as arm and chromosome level CNAs. For 29 patients only targeted sequencing data were
526 available while 20 patients had one WGS tumor and at least one tumor sequenced by targeted
527 sequencing. Additional alterations detected by WGS but cannot be captured by MSK-IMPACT (i.e. SVs
528 at loci such as *TERT* and *FOXR1*) are not included in this analysis (indicated with
529 SUBCLONE_TYPE==NA in Supplementary Table 2).

530

531 For this patient subset, clonal structure was first analyzed with the allele-specific CNA data as
532 assessed using FACETS⁷⁹ in targeted data and Battenberg in WGS data. CNA-based phylogenies were
533 derived by comparing the genomewide CNAs of the tumors as well as using MEDICC2 with default
534 parameters. Substitutions and indels were analyzed together using DriverClone
535 [<https://github.com/papaemmelab/driverclone>], an inhouse algorithm designed for studying clonal
536 structure specifically from sparse targeted sequencing data. Briefly, DriverClone first derives a
537 posterior probability for the CCF of each variant, taking into account information on local ploidy,
538 coverage, tumor purity and possible genotypes. DriverClone then clusters the variants in CCF space
539 using a weighted variant graph where edges represent overlaps of posterior credible intervals
540 between variant pairs in each sample. Low weight edges are pruned. A depth-first search then finds
541 all connected components in the variant graph and retrieves clusters of variants belonging to the
542 same predicted clone. To enable probabilistic clonal ordering with few observations per clone,
543 DriverClone extends the non-parametric bootstrapping model of ClonEvol so that bootstrap samples
544 are obtained from a mixture distribution of variant posteriors. A tree enumeration algorithm
545 (originally implemented in Clonevol) then identifies all possible tumor phylogenies that fulfill the
546 appropriate biological constraints. Phylogenies predicted from this analysis are displayed in the
547 Supplementary Figs. 48-53.

548

549 **Timing the emergence of MRCA**

550 Timing of the MRCA emergence was performed in a subset of 39 patients with ≥ 2 WGS tumors
551 where at least one tumor was from a pre-treatment diagnostic specimen or therapy resection.
552 Association between age at diagnosis and trunk length was assessed by a linear regression model
553 using R *lm* function and in a multivariate analysis using R *glm* function taking into account disease
554 subtype, stage at diagnosis and number of WGS tumors. MRCA analysis was done using a previously

555 published analysis workflow³⁷ in two steps 1) First patient-specific mutation rates were estimated
556 via linear mixed effect modeling with the number of mutations attributed to the clock-like mutational
557 signature SBS40. 2) Patient-specific mutation rates and the number of SBS40 mutations on the trunk
558 were used to estimate the time of emergence for MRCA applying a bootstrapping approach to
559 estimate 95% confidence intervals (CIs). MRCA was classified as ‘pre-natal’ if CIs overlapped the time
560 of birth and ‘post-natal’ otherwise.

561

562 **Analysis of truncal and subclonal somatic changes**

563 This analysis was performed in a subset of 94 patients with two or more tumors for which WGS
564 and/or targeted sequencing data was used to assess genome-wide segmental CNAs and oncogenic
565 substitution, indels, CNAs and SVs in reported ~450 cancer genes included in targeted sequencing
566 panel. Detailed analysis of *MYCN* and *TERT* loci was performed in 13 and 7 patients, respectively,
567 with two or more WGS samples available.

568

569 **Analysis of evolutionary patterns**

570 Analysis of divergence in the primary site was performed in a subset of 30 patients with two or more
571 tumors from the primary site available. Divergence is defined as acquisition of recurrent CNAs as well
572 as oncogenic mutations provided in Supplementary Table 2. Comparison of primary site to
573 disseminated disease was performed in a subset of 9 patients with two or more tumors from the
574 primary site and tumor(s) from disseminated sites. Timing of metastasis with respect to therapy was
575 performed in a subset of 13 patients for whom at least one tumor from the primary site and two or
576 more tumors from local-regional and/or distant metastatic sites were sequenced by WGS. Lineage
577 relationship between local-regional and/or distant metastatic tumors was studied in a subset of 19
578 patients with at least one tumor from the primary site as well as local-regional and/or distant
579 metastatic tumors available.

580

581 **Author contributions**

582

583 E.P., N.K.C and G.G. designed the study. G.G., M.F.L., J.S.M.M, J.E.A.O and J.Z. developed algorithmic
584 infrastructure and G.G. performed bioinformatic analysis with support from L.C., M.R. and G.A.. N.K.C,
585 S.S.R., B.S., M.P.L, B.H.K, S.M. and N.S. performed the clinical management of the patients. N.K.C and
586 N.B. performed patient consent. N.K.C oversaw biospecimen banking performed by I.Y.C and Y.F.
587 while D.Y. and F.D.C executed laboratory processing of PDX specimens. N.K.C. collected clinical data
588 for the patients. C.A.I.O. led the clinical donation program. G.G. prepared figures and tables. G.G., N.K.C.
589 and E.P. reviewed analysis results and interpretation of findings and wrote the manuscript with input
590 from D.B.S., B.H.K., S.M., C.A.I.D and A.K.. All authors reviewed and approved the manuscript for
591 submission.

592 **ACKNOWLEDGEMENTS**

593 The authors would like to acknowledge Drs T. Heaton, and J. Gerstle for their surgical expertise in
594 specimen collections. Dr David Wedge and Dr Maire Ni Leathlobhair of Big Data Institute, University
595 of Oxford, UK, for support and interesting discussions, members of MSK integrative Genomics
596 Operation core for sample processing and sequencing. N-K.C. was partly supported by the Enid Haupt
597 Endowed Chair, the Robert Steel Foundation, Katie Find a Cure, and the Catie Hoch Foundation in
598 building the neuroblastoma tumor tissue archive. E.P. is a Josie Robertson Investigator and is
599 supported by the European Hematology Association, American Society of Hematology, Gabrielle's
600 Angels Foundation, V Foundation and The Geoffrey Beene Foundation and a Damon-Runyon Rachleff
601 Innovator Award recipient. Funding for this study was supported by the Olayan Fund for Precision
602 Pediatric Cancer Medicine.

603

604 **CONFLICT OF INTEREST**

605 G.G. is a consultant in Isabl Inc. E.P., A.K. and J.S.M.M are founders, equity holders and hold
606 fiduciary roles in Isabl Inc. NKC reports receiving commercial research grants unrelated to this
607 study, from Y-mabs Therapeutics and Abpro-Labs Inc.; holding ownership interest/equity in Y-
608 Mabs Therapeutics Inc., holding ownership interest/equity in Abpro-Labs, and owning stock
609 options in Eureka Therapeutics. N-K.C. is the inventor and owner of issued patents, some licensed
610 by MSK to Ymabs Therapeutics, Biotec Pharmacon, and Abpro-labs. N-K.C. is an advisory board
611 member for Abpro-Labs and Eureka Therapeutics. MSK also has financial interest in Y-mabs.

612

613 **Data availability**

614 All data is available in dbGAP (in submission) and cbioPortal.

615 **Code availability**

616 Additional scripts and data used for generating the figures are available at
617 [https://github.com/gg10/gg10-Clonal-evolution-during-metastatic-spread-in-high-risk-](https://github.com/gg10/gg10-Clonal-evolution-during-metastatic-spread-in-high-risk-neuroblastoma)
618 [neuroblastoma](https://github.com/gg10/gg10-Clonal-evolution-during-metastatic-spread-in-high-risk-neuroblastoma).

619

620 **Bibliography**

- 621 1. Maris, J. M. Recent Advances in Neuroblastoma. *New England Journal of Medicine* vol. 362
622 2202–2211 (2010).
- 623 2. London, W. B. *et al.* Historical time to disease progression and progression-free survival in
624 patients with recurrent/refractory neuroblastoma treated in the modern era on Children’s
625 Oncology Group early-phase trials. *Cancer* vol. 123 4914–4923 (2017).
- 626 3. Abbasi, M. R. *et al.* Impact of Disseminated Neuroblastoma Cells on the Identification of the
627 Relapse-Seeding Clone. *Clin. Cancer Res.* **23**, 4224–4232 (2017).

- 628 4. Eleveld, T. F. *et al.* Relapsed neuroblastomas show frequent RAS-MAPK pathway mutations.
629 *Nat. Genet.* **47**, 864–871 (2015).
- 630 5. Schramm, A. *et al.* Mutational dynamics between primary and relapse neuroblastomas. *Nat.*
631 *Genet.* **47**, 872–877 (2015).
- 632 6. Chicard, M. *et al.* Genomic Copy Number Profiling Using Circulating Free Tumor DNA Highlights
633 Heterogeneity in Neuroblastoma. *Clin. Cancer Res.* **22**, 5564–5573 (2016).
- 634 7. Van Roy, N. *et al.* Shallow Whole Genome Sequencing on Circulating Cell-Free DNA Allows
635 Reliable Noninvasive Copy-Number Profiling in Neuroblastoma Patients. *Clin. Cancer Res.* **23**,
636 6305–6314 (2017).
- 637 8. Chicard, M. *et al.* Whole-Exome Sequencing of Cell-Free DNA Reveals Temporo-spatial
638 Heterogeneity and Identifies Treatment-Resistant Clones in Neuroblastoma. *Clin. Cancer Res.*
639 **24**, 939–949 (2018).
- 640 9. Fransson, S. *et al.* Whole-genome sequencing of recurrent neuroblastoma reveals somatic
641 mutations that affect key players in cancer progression and telomere maintenance. *Sci. Rep.* **10**,
642 22432 (2020).
- 643 10. Karlsson, J. *et al.* Four evolutionary trajectories underlie genetic intratumoral variation in
644 childhood cancer. *Nat. Genet.* **50**, 944–950 (2018).
- 645 11. Andersson, N. *et al.* Extensive Clonal Branching Shapes the Evolutionary History of High-Risk
646 Pediatric Cancers. *Cancer Res.* **80**, 1512–1523 (2020).
- 647 12. Schmelz, K. *et al.* Spatial and temporal intratumour heterogeneity has potential consequences
648 for single biopsy-based neuroblastoma treatment decisions. *Nat. Commun.* **12**, 6804 (2021).
- 649 13. Peifer, M. *et al.* Telomerase activation by genomic rearrangements in high-risk neuroblastoma.
650 *Nature* **526**, 700–704 (2015).
- 651 14. Brady, S. W. *et al.* Pan-neuroblastoma analysis reveals age- and signature-associated driver
652 alterations. *Nat. Commun.* **11**, 5183 (2020).

- 653 15. Monclair, T. *et al.* The International Neuroblastoma Risk Group (INRG) staging system: an INRG
654 Task Force report. *J. Clin. Oncol.* **27**, 298–303 (2009).
- 655 16. Pugh, T. J. *et al.* The genetic landscape of high-risk neuroblastoma. *Nat. Genet.* **45**, 279–284
656 (2013).
- 657 17. Valentijn, L. J. *et al.* TERT rearrangements are frequent in neuroblastoma and identify
658 aggressive tumors. *Nat. Genet.* **47**, 1411–1414 (2015).
- 659 18. Amoroso, L. *et al.* Genomic coamplification of CDK4/MDM2/FRS2 is associated with very poor
660 prognosis and atypical clinical features in neuroblastoma patients. *Genes Chromosomes Cancer*
661 **59**, 277–285 (2020).
- 662 19. Alexandrov, L. B. *et al.* The repertoire of mutational signatures in human cancer. *Nature* **578**,
663 94–101 (2020).
- 664 20. Alexandrov, L. B. *et al.* Signatures of mutational processes in human cancer. *Nature* **500**, 415–
665 421 (2013).
- 666 21. Kucab, J. E. *et al.* A Compendium of Mutational Signatures of Environmental Agents. *Cell* **177**,
667 821–836.e16 (2019).
- 668 22. Wang, T. *et al.* MYCN drives glutaminolysis in neuroblastoma and confers sensitivity to an ROS
669 augmenting agent. *Cell Death & Disease* vol. 9 (2018).
- 670 23. Gröbner, S. N. *et al.* The landscape of genomic alterations across childhood cancers. *Nature*
671 **555**, 321–327 (2018).
- 672 24. Ma, X. *et al.* Pan-cancer genome and transcriptome analyses of 1,699 paediatric leukaemias and
673 solid tumours. *Nature* **555**, 371–376 (2018).
- 674 25. Wei, J. S. *et al.* Clinically Relevant Cytotoxic Immune Cell Signatures and Clonal Expansion of T-
675 Cell Receptors in High-Risk MYCN-Not-Amplified Human Neuroblastoma. *Clinical Cancer*
676 *Research* vol. 24 5673–5684 (2018).
- 677 26. Layer, J. P. *et al.* Amplification of N-Myc is associated with a T-cell-poor microenvironment in

- 678 metastatic neuroblastoma restraining interferon pathway activity and chemokine expression.
679 *Oncoimmunology* **6**, e1320626 (2017).
- 680 27. Georger, B. *et al.* Pembrolizumab in paediatric patients with advanced melanoma or a PD-L1-
681 positive, advanced, relapsed, or refractory solid tumour or lymphoma (KEYNOTE-051): interim
682 analysis of an open-label, single-arm, phase 1–2 trial. *The Lancet Oncology* vol. 21 121–133
683 (2020).
- 684 28. Georger, B. *et al.* Atezolizumab for children and young adults with previously treated solid
685 tumours, non-Hodgkin lymphoma, and Hodgkin lymphoma (iMATRIX): a multicentre phase 1–
686 2 study. *The Lancet Oncology* vol. 21 134–144 (2020).
- 687 29. Davis, K. L. *et al.* Nivolumab in children and young adults with relapsed or refractory solid
688 tumours or lymphoma (ADVL1412): a multicentre, open-label, single-arm, phase 1-2 trial.
689 *Lancet Oncol.* **21**, 541–550 (2020).
- 690 30. Havel, J. J., Chowell, D. & Chan, T. A. The evolving landscape of biomarkers for checkpoint
691 inhibitor immunotherapy. *Nat. Rev. Cancer* **19**, 133–150 (2019).
- 692 31. Pich, O. *et al.* The mutational footprints of cancer therapies. *Nat. Genet.* **51**, 1732–1740 (2019).
- 693 32. Angus, L. *et al.* The genomic landscape of metastatic breast cancer highlights changes in
694 mutation and signature frequencies. *Nat. Genet.* **51**, 1450–1458 (2019).
- 695 33. Kocakavuk, E. *et al.* Radiotherapy is associated with a deletion signature that contributes to
696 poor outcomes in patients with cancer. *Nat. Genet.* **53**, 1088–1096 (2021).
- 697 34. Behjati, S. *et al.* Mutational signatures of ionizing radiation in second malignancies. *Nat.*
698 *Commun.* **7**, 12605 (2016).
- 699 35. Gerstung, M. *et al.* The evolutionary history of 2,658 cancers. *Nature* **578**, 122–128 (2020).
- 700 36. Mitchell, T. J. *et al.* Timing the Landmark Events in the Evolution of Clear Cell Renal Cell Cancer:
701 TRACERx Renal. *Cell* **173**, 611–623.e17 (2018).
- 702 37. Rustad, E. H. *et al.* Timing the initiation of multiple myeloma. *Nat. Commun.* **11**, 1917 (2020).

- 703 38. Coorens, T. H. H. *et al.* Inherent mosaicism and extensive mutation of human placentas. *Nature*
704 **592**, 80–85 (2021).
- 705 39. Schleiermacher, G. *et al.* Emergence of new ALK mutations at relapse of neuroblastoma. *J. Clin.*
706 *Oncol.* **32**, 2727–2734 (2014).
- 707 40. Althoff, K. *et al.* A Cre-conditional MYCN-driven neuroblastoma mouse model as an improved
708 tool for preclinical studies. *Oncogene* **34**, 3357–3368 (2015).
- 709 41. Schwab, M. *et al.* Amplified DNA with limited homology to myc cellular oncogene is shared by
710 human neuroblastoma cell lines and a neuroblastoma tumour. *Nature* vol. 305 245–248
711 (1983).
- 712 42. Kohl, N. E. *et al.* Transposition and amplification of oncogene-related sequences in human
713 neuroblastomas. *Cell* **35**, 359–367 (1983).
- 714 43. Cobrinik, D. *et al.* Recurrent pre-existing and acquired DNA copy number alterations, including
715 focal TERT gains, in neuroblastoma central nervous system metastases. *Genes Chromosomes*
716 *Cancer* **52**, 1150–1166 (2013).
- 717 44. Cheung, N.-K. V. *et al.* Association of age at diagnosis and genetic mutations in patients with
718 neuroblastoma. *JAMA* **307**, 1062–1071 (2012).
- 719 45. Franks, L. M., Bollen, A., Seeger, R. C., Stram, D. O. & Matthay, K. K. Neuroblastoma in adults and
720 adolescents: an indolent course with poor survival. *Cancer* **79**, 2028–2035 (1997).
- 721 46. Ackermann, S. *et al.* A mechanistic classification of clinical phenotypes in neuroblastoma.
722 *Science* **362**, 1165–1170 (2018).
- 723 47. Carr-Wilkinson, J. *et al.* High Frequency of p53/MDM2/p14ARF Pathway Abnormalities in
724 Relapsed Neuroblastoma. *Clin. Cancer Res.* **16**, 1108–1118 (2010).
- 725 48. DuBois, S. G. *et al.* Metastatic sites in stage IV and IVS neuroblastoma correlate with age, tumor
726 biology, and survival. *J. Pediatr. Hematol. Oncol.* **21**, 181–189 (1999).
- 727 49. Yates, L. R. & Campbell, P. J. Evolution of the cancer genome. *Nat. Rev. Genet.* **13**, 795–806

- 728 (2012).
- 729 50. Landau, H. J. *et al.* Accelerated single cell seeding in relapsed multiple myeloma. *Nat. Commun.*
730 **11**, 3617 (2020).
- 731 51. Berlanga, P. *et al.* Central nervous system relapse in high-risk stage 4 neuroblastoma: The HR-
732 NBL1/SIOPEN trial experience. *Eur. J. Cancer* **144**, 1–8 (2021).
- 733 52. Ishida, M. *et al.* Sprouty2 regulates growth and differentiation of human neuroblastoma cells
734 through RET tyrosine kinase. *Cancer Sci.* **98**, 815–821 (2007).
- 735 53. Gundem, G. *et al.* The evolutionary history of lethal metastatic prostate cancer. *Nature* **520**,
736 353–357 (2015).
- 737 54. Keshelava, N. *et al.* Loss of p53 function confers high-level multidrug resistance in
738 neuroblastoma cell lines. *Cancer Res.* **61**, 6185–6193 (2001).
- 739 55. van Groningen, T. *et al.* Neuroblastoma is composed of two super-enhancer-associated
740 differentiation states. *Nat. Genet.* **49**, 1261–1266 (2017).
- 741 56. Koche, R. P. *et al.* Extrachromosomal circular DNA drives oncogenic genome remodeling in
742 neuroblastoma. *Nat. Genet.* **52**, 29–34 (2020).
- 743 57. Kim, H. *et al.* Extrachromosomal DNA is associated with oncogene amplification and poor
744 outcome across multiple cancers. *Nat. Genet.* **52**, 891–897 (2020).
- 745 58. Kushner, B. H. *et al.* Efficacy of naxitamab in patients with refractory/relapse (R/R) high-risk
746 neuroblastoma (HR-NB) by bone/bone marrow (BM) evaluation, potential sites of residual
747 disease. *Journal of Clinical Oncology* vol. 39 10022–10022 (2021).
- 748 59. Yarmarkovich, M. *et al.* Cross-HLA targeting of intracellular oncoproteins with peptide-centric
749 CARs. *Nature* (2021) doi:10.1038/s41586-021-04061-6.
- 750 60. Diolaiti, D. *et al.* A recurrent novel MGA–NUTM1 fusion identifies a new subtype of high-grade
751 spindle cell sarcoma. *Molecular Case Studies* vol. 4 a003194 (2018).
- 752 61. Zehir, A. *et al.* Mutational landscape of metastatic cancer revealed from prospective clinical

- 753 sequencing of 10,000 patients. *Nat. Med.* **23**, 703–713 (2017).
- 754 62. Chakravarty, D. *et al.* OncoKB: Annotation of the oncogenic effect and treatment implications of
755 somatic mutations in cancer. *Journal of Clinical Oncology* vol. 34 11583–11583 (2016).
- 756 63. Medina-Martínez, J. S. *et al.* Isabl Platform, a digital biobank for processing multimodal patient
757 data. *BMC Bioinformatics* vol. 21 (2020).
- 758 64. Landrum, M. J. *et al.* ClinVar: public archive of interpretations of clinically relevant variants.
759 *Nucleic Acids Res.* **44**, D862–8 (2016).
- 760 65. Forbes, S. A. *et al.* COSMIC: somatic cancer genetics at high-resolution. *Nucleic Acids Res.* **45**,
761 D777–D783 (2017).
- 762 66. Karczewski, K. J. *et al.* The mutational constraint spectrum quantified from variation in
763 141,456 humans. *Nature* **581**, 434–443 (2020).
- 764 67. McLaren, W. *et al.* The Ensembl Variant Effect Predictor. *Genome Biol.* **17**, 122 (2016).
- 765 68. Srivastava, A. *et al.* Alignment and mapping methodology influence transcript abundance
766 estimation. *Genome Biol.* **21**, 239 (2020).
- 767 69. John, C. R. *et al.* M3C: Monte Carlo reference-based consensus clustering. *Sci. Rep.* **10**, 1816
768 (2020).
- 769 70. Korotkevich, G. *et al.* Fast gene set enrichment analysis. doi:10.1101/060012.
- 770 71. Bagaev, A. *et al.* Conserved pan-cancer microenvironment subtypes predict response to
771 immunotherapy. *Cancer Cell* **39**, 845–865.e7 (2021).
- 772 72. Aran, D., Hu, Z. & Butte, A. J. xCell: digitally portraying the tissue cellular heterogeneity
773 landscape. *Genome Biol.* **18**, 220 (2017).
- 774 73. Alexandrov, L. B., Nik-Zainal, S., Wedge, D. C., Campbell, P. J. & Stratton, M. R. Deciphering
775 signatures of mutational processes operative in human cancer. *Cell Rep.* **3**, 246–259 (2013).
- 776 74. Blokzijl, F., Janssen, R., van Boxtel, R. & Cuppen, E. MutationalPatterns: comprehensive
777 genome-wide analysis of mutational processes. *Genome Med.* **10**, 33 (2018).

- 778 75. Li, Y. *et al.* Patterns of somatic structural variation in human cancer genomes. *Nature* **578**,
779 112–121 (2020).
- 780 76. Cortés-Ciriano, I. *et al.* Comprehensive analysis of chromothripsis in 2,658 human cancers
781 using whole-genome sequencing. *Nat. Genet.* **52**, 331–341 (2020).
- 782 77. Nik-Zainal, S. *et al.* The life history of 21 breast cancers. *Cell* **149**, 994–1007 (2012).
- 783 78. Dang, H. X. *et al.* ClonEvol: clonal ordering and visualization in cancer sequencing. *Ann. Oncol.*
784 **28**, 3076–3082 (2017).
- 785 79. Shen, R. & Seshan, V. E. FACETS: allele-specific copy number and clonal heterogeneity analysis
786 tool for high-throughput DNA sequencing. *Nucleic Acids Res.* **44**, e131 (2016).
- 787 80. Detro, S. C., Wedge, D. C. & Van Loo, P. Principles of Reconstructing the Subclonal Architecture
788 of Cancers. *Cold Spring Harb. Perspect. Med.* **7**, (2017).

789 **Figure legends**

790 **Figure 1. Patient cohort and genome-wide mutational landscape. a)** Barplot shows the number
791 of tumors sequenced from 94 patients with two or more samples color-coded by type of
792 sample and sequencing performed. Patients are shown as columns organized by the disease
793 subtype which are as follows: 1) MCYN, patients with *MYCN* amplification. 2) TERT, patients
794 with *TERT* SVs. 3) ATRX, patients with *ATRX* events. 4) MDM2-CDK4, patients with *MDM2*-
795 *CDK4* co-amplifications. 5) SEG-CNA and 6) CUM-CNA, patients with segmental or numeric
796 CNAs but without the aforementioned alterations. (SV, structural variants. CNA, copy number
797 aberration. WGS, whole genome sequencing.). Information about age and stage at diagnosis is
798 provided as tile plots at the bottom. Box plots show comparison of the proportion of mutations
799 attributed to SBS18 and SBS40 **(b)** and tumor mutation burden (TMB) **(c)** in WGS data across
800 diagnostic tumors of different molecular subtypes (n=72 tumors). **d)** Box plot on the left shows
801 the increase in TMB across samples collected at diagnosis, t-resection, relapse and further

802 relapse (n=129 patients) while on the right is the fold change in TMB in relapse and further
803 relapse samples compared to the matched diagnostic tumor of the same patient (n=22
804 patients). **e)** Box plots show the proportion of substitutions attributed to SBS31, SBS35 and
805 temozolomide (TMZ) signatures across samples collected at diagnosis, t-resection, relapse and
806 further relapse (n=129 patients). **f)** Boxplots show the number of substitutions attributed to
807 therapy-related mutational signatures for tumors from patients with stage-4 disease who were
808 exposed to increasing numbers of rounds of platinum or temozolomide-based chemotherapy
809 (n=145 tumors). The data and script for Fig. 1 are available in Supplementary Table 1 and the
810 GitHub repository.

811 **Figure 2. Timing of emergence of the first malignant clone. a)** Scatter plot shows the
812 relationship between the number of single nucleotide variants (SNVs) on the trunk (trunk
813 length) and age at diagnosis (Pearson correlation). **b)** Barplots show the breakdown of upper,
814 middle and lower tertiles of the trunk length distribution by stage at diagnosis. **c)** Timeline plot
815 shows the time of diagnosis and the predicted time of emergence of the most recent common
816 ancestor (MRCA) with 95% confidence intervals for n=39 patients. Number of SBS40-
817 associated SNVs on the trunk is shown next to the patient id. Shaded area from -9 to 0 on the
818 x-axis shows the period in utero. The predicted time of emergence of the MRCA is shown with a
819 circle (pre-natal) or a triangle (post-natal). **d)** Ternary plot shows the proportion of events that
820 are shared by all tumors of a patient, seen in a subclone specific to a sample from the primary
821 site or metastatic/relapse site. Dots are color-coded red or green to indicate a tendency to be
822 shared or metastasis/relapse-specific with a size proportional to the total number of events. **e)**
823 Heatmap shows the number of truncal and subclonal genetic changes identified in 94 patients
824 with ≥ 2 tumors. Mutations and SVs are collapsed to the affected pathways except for those
825 hitting the most recurrent disease-defining genes (*MYCN*, *TERT* and *ATRX*). Black dots indicate
826 parallel evolution while crosses indicate the loci affected by continuous subclonal SVs when

827 there is already an SV event on the trunk of the patient. Lowermost tile plot shows the
828 availability of multi-WGS data, number of tumors and the timepoints studied for each patient.
829 Barplot on the left shows the frequency of the events per row. +, gain. -, loss. The data and
830 script for Fig. 2 are available in Supplementary Tables 1, 2 and 4 and the GitHub repository.

831 **Figure 3. Subtype-specific evolutionary trajectories. a)** Subclonal structure for patient H103207

832 is summarized in multiple panels. Treatment timeline gives a summary of the therapy
833 administered, the sequenced tumors and the survival status at last followup. Body map shows
834 the location of the tumor sites sequenced. Subclone tree shows the lineage relationships
835 amongst the subclones identified in a patient. Subclones are designated by branches with non-
836 informative lengths. Trunk is shown in gray at the top of the tree. Terminal nodes are
837 annotated with tumors where the corresponding clone is present. Branches are annotated
838 with putative oncogenic events. Different types of *MYCN* amplicons are indicated by a number
839 after gene name (i.e. *MYCN.1*). Continuous accumulation of SVs at *MYCN* loci is indicated by
840 stars (*). On the right, *MYCN* locus for each tumor is shown with an integrated copy number
841 (CN)/structural variant (SV) plot with absolute copy number on the y-axis and SVs as arcs
842 color-coded by the subclones they were assigned to. *ALK^{ECD}*, *ALK* with a deletion of exons
843 encoding the extra-cellular domain. **b)** Treatment timeline, subclone tree and body map as
844 described in Fig-3a are shown for patient H132384. Evolution at *MDM2*, *CDK4* and *TERT* loci
845 are shown in the integrated CN/SV plot as described in Fig. 3a. Barplot shows the increase in
846 expression in the tumors with *TERT* SVs. **c)** Treatment timeline, subclone tree and body maps
847 as described in Fig-3a are shown for two different *ATRX*-mutant patients. **d)** Treatment
848 timeline, subclone tree and body maps as described in Fig-3a are shown for two patients with
849 *TP53* mutations. Detailed description of each patient is provided in Supplementary
850 Information. The data for Fig. 3 are available as raw data at dbGAP and scripts are available
851 through ISABL platform.

852 **Figure 4. Timing of metastasis. a)** Subclonal structure for patient H118706 is shown. Treatment
853 timeline is as described in Fig. 3a. On the right is the signature tree with the results from the
854 subclone-specific mutational signature analysis across the subclone tree of the patient. Each
855 subclone is shown as a stacked bar plot showing the proportion of the mutations attributed to
856 the six different mutational signatures and with total length proportional to the number of
857 substitutions in the corresponding subclone. Branches are separated by a dashed line and
858 annotated with the putative oncogenic changes assigned to the corresponding subclone.
859 Terminal nodes are annotated with tumors where the corresponding clone is present.
860 Triangles denote the subclones involved in metastatic spread where gray and white indicate
861 spread before and after therapy, respectively. The id of the metastatic subclones is annotated
862 next to the corresponding branch. Body maps show the possible movement of subclones
863 involved in spread before and after therapy indicated by the subclone ids next to the body
864 maps. Subclones are color-coded according to the clonal phylogeny shown in the legend.
865 Details of the clonal and genomic for H118706 is provided in Supplementary Information. **b)**
866 Left barplot shows the proportion of different types of clonal transitions from diagnosis to first
867 relapse (n=47) and between consecutive relapses (n=67) while the right barplot gives a
868 breakdown of clonal transitions across different disease subtypes. The different types of
869 transitions are 1) 'same' where the relapse is caused by the same clone as the previous time
870 point with no new genetic changes acquired. 2) 'earlier' where the relapse is caused by an
871 earlier clone in the phylogenetic tree. 3) 'linear' where the relapse is caused by a clone with
872 new CNAs and oncogenic mutations/SVs while no such events are seen in the clone specific to
873 the previous time point. 4) 'branched' where clones from both time points have genetic
874 changes. **c)** Barplot shows the number of different types of clonal transitions where the
875 relapsing clone has genetic changes affecting the listed CNAs and oncogenic mutations
876 collapsed to pathways affected except for those mutations affecting the most frequent disease-

877 defining genes (*MYCN*, *TERT* and *ATRX*). The inner plot shows the pathways affected by parallel
878 events across clonal transitions that switch between lineages. **d** and **e**) Subclonal structure for
879 patients H134819 and H134821 are shown. Body maps and treatment timelines are as
880 described in Fig. 3a. Signature trees are as described in Fig. 4a. For H134821 the left body map
881 shows the local-regional spread before therapy while the right body map shows the spread 9
882 years after diagnosis. Detailed description of each patient is provided in Supplementary
883 Information. The data for Fig. 4a, d and e are available as raw data at dbGAP and scripts are
884 available through ISABL platform while data and scripts for Fig. 4b-c are available in
885 Supplementary Table 6 and the GitHub repository.

886 **Figure 5. Complex seeding patterns after therapy.** Subclonal structures for patients H103207
887 **(a)**, H134722 **(b)** and H132374 **(c)** are shown with treatment timeline and signature tree as
888 described in Fig. 3a and Fig. 4a, respectively. Detailed description of each patient is provided in
889 Supplementary Information. **a)** Body map on the left shows the seeding events before
890 diagnosis in H103207. Body map on the right depicts the polyclonal seeding after therapy
891 amongst liver and bilateral lungs involving subclones 5 and 8. **b)** The left body map shows the
892 spread before therapy. The black arc indicates the distinct subclone in R1 left lung metastasis
893 sequenced with MSK-IMPACT. The right body map shows subclones 2, 3, 4, 7 and 10 involved
894 in polyclonal seeding across locoregional and metastatic sites in H134722. *TP53* substitution
895 assigned to subclone-7 is also found in PDX modeling of R3, R4, R8, R9, R10 and R11. **c)** Body
896 maps depict two different scenarios that explain the subclonal structure in H132374: The left
897 body map shows possible polyclonal seeding in the CNS by a mixture of subclones 3 and 4. In
898 this scenario lung metastasis is caused by subclone-4 after platinum chemotherapy. Shown on
899 the right body map is the second scenario of met-to-met seeding from CNS to lung by subclone-
900 4 after therapy. The data for Fig. 5 are available as raw data at dbGAP and scripts are available
901 through ISABL platform.

902 **Extended Data Figure 1. Summary of mutation calling and genomic landscape. a)** Barplots
903 show the number of substitutions, indels and SVs identified in WGS tumors (n=247) in the
904 cohort grouped by the different disease subtypes and color-coded by the sample type. **b)**
905 Barplots show the prevalence of segmental CNAs and genes affected by mutations and SVs
906 across the cohort (n=470 tumors). Only genes affected in at least two patients are shown.
907 Bottom bar plot gives a summary of the type of mutations for each CNA/gene. CNA, copy
908 number aberration. Complex, small complex insertion/deletion. Del, small deletion. Ins, small
909 insertion. Sub, substitution. SV, structural variant. **c)** Survival plot shows the clinical outcome
910 of *MYCN-A* patients (n=68) with *TERT*_p substitutions, *TERT-SV* or no *TERT* events with 95%
911 confidence intervals. P-value from coxph analysis taking into account age at diagnosis is
912 shown. **d)** Heatmap gives a summary of the co-mutation patterns in the current cohort with
913 the frequency of events in the upper triangle and odds ratios in the lower triangle. Only odds
914 ratios with p values <0.05 are colored in shades of blue for co-mutation or red for mutually
915 exclusive interactions. Significant interactions are indicated with a star or a dot according to
916 the significance level. FDR, false discovery rate. FWER, family-wise error rate. The data and
917 script for Extended Fig. 1 are available in Supplementary Tables 1-2 and the GitHub repository.

918 **Extended Data Figure 2. Summary of mutational signature analyses in the current WGS data.**

919 **a)** 96 mutational contexts for the substitution signatures identified de novo are shown as the
920 barplots on the left while the reference signatures from COSMIC.v3 are shown in the barplot in
921 the middle. Right barplot shows the prevalence of different types of indels amongst the indel
922 signatures identified de novo. **b)** Heatmap shows the proportions of substitutions at 96
923 mutational contexts for each WGS tumor (n=247) shown in rows together with sample type,
924 disease subtype, platinum, temozolomide and radiotherapy status on the left and number of
925 substitutions and indels and exposure to identified signatures in substitution and indel data on
926 the right. The data and script for Extended Fig. 2 are available at the GitHub repository.

927 **Extended Data Figure 3. Biological and clinical correlates of mutational patterns. a)** Scatter
928 plots show the association between exposure to SBS18 (left) or SBS40 (right) and age at
929 diagnosis amongst the diagnostic/t-resection tumors (Pearson correlation). **b)** Box plot shows
930 the mean expression of the genes in glutaminolysis signature associated with ROS
931 accumulation²² across diagnostic tumors of different disease subtypes (left) and *MYCN-A*
932 tumors from diagnosis, t-resection and relapse and further relapses (right). Comparisons with
933 significant p-values are shown. **c)** Scatter plot on the left shows correlation between number of
934 SNVs and the number of predicted neoantigens while the scatter plot on the right shows the
935 relationship between the number of predicted neoantigens and immune infiltrates in the
936 surrounding tumor microenvironment as assessed from RNAseq (Pearson correlation). **d)**
937 Barplots show the proportion of genome-wide SNVs (left) and oncogenic driver SNVs (right)
938 attributed to different mutational signatures broken down by presence in post-therapy relapse
939 tumors. The data and script for Extended Fig. 3 are available in Supplementary Table 1 and the
940 GitHub repository.

941 **Extended Data Figure 4-5. Subclone trees for 94 neuroblastoma patients with two or more**
942 **tumors sequenced.** Each tree shows the subclonal structure in an individual patient. Patients
943 are organized according to disease subtype and the availability of tumors from primary site
944 (diagnosis/reresection/t-resection) and relapses. Branches are annotated with recurrent CNAs
945 and oncogenic mutations/SVs and colored according to the latest tumor they were identified in
946 1) blue for subclones specific to a diagnostic tumor 2) light blue for subclones seen in
947 reresections 3) green for subclones seen in a t-resection tumor 4) orange for subclones seen in
948 a relapse tumor and 5) red for subclones seen in a further relapse tumor. Subclonal events at
949 *MYCN*, *TERT* and *ATRX* loci are shown in red font. Events with which clonal status cannot be
950 determined are indicated with a question mark. Different evolutionary patterns are indicated
951 with an icon next to the patient id. Tumor sites and the type of sequencing are indicated below

952 the trees. G, whole-genome sequencing. T, targeted sequencing. B, both. For H103207,
953 H118706 and H134819 a simplified version of the tree is shown due to space. Detailed analysis
954 of subclonal structure for 94 patients is provided in Supplementary Fig. 2-46 and 48-53. The
955 data Extended Figs. 4-5 are available in Supplementary Table 5 and the scripts are available
956 through the ISABL platform.

957 **Extended Data Figure 6. Timing of metastasis.** Signatures trees as described in Fig-4a are
958 shown for 13 patients with one or more tumors from the primary site and two or more tumors
959 from locoregional and/or distant metastasis. Patients in the top row have at least one tumor
960 from distant metastatic site while patients in the bottom row have locoregional relapses only.
961 The subclones involved in disease spread from the primary are indicated with a black arrow
962 while the daughter clones are shown with red arrows. The data for Extended Fig. 6 are
963 available as raw data at dbGAP and the scripts are available through the ISABL platform.

964

965

966

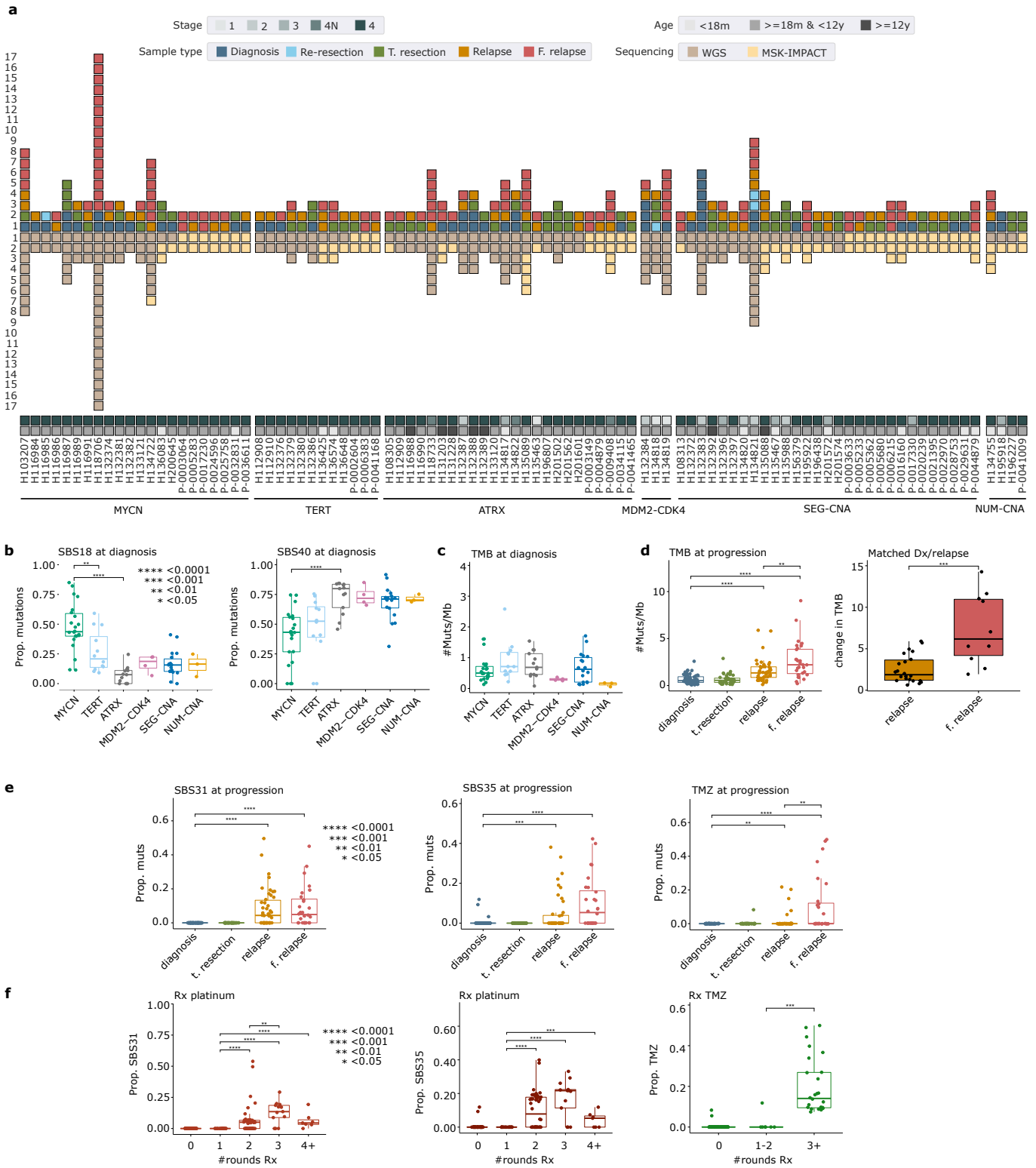


Figure 2

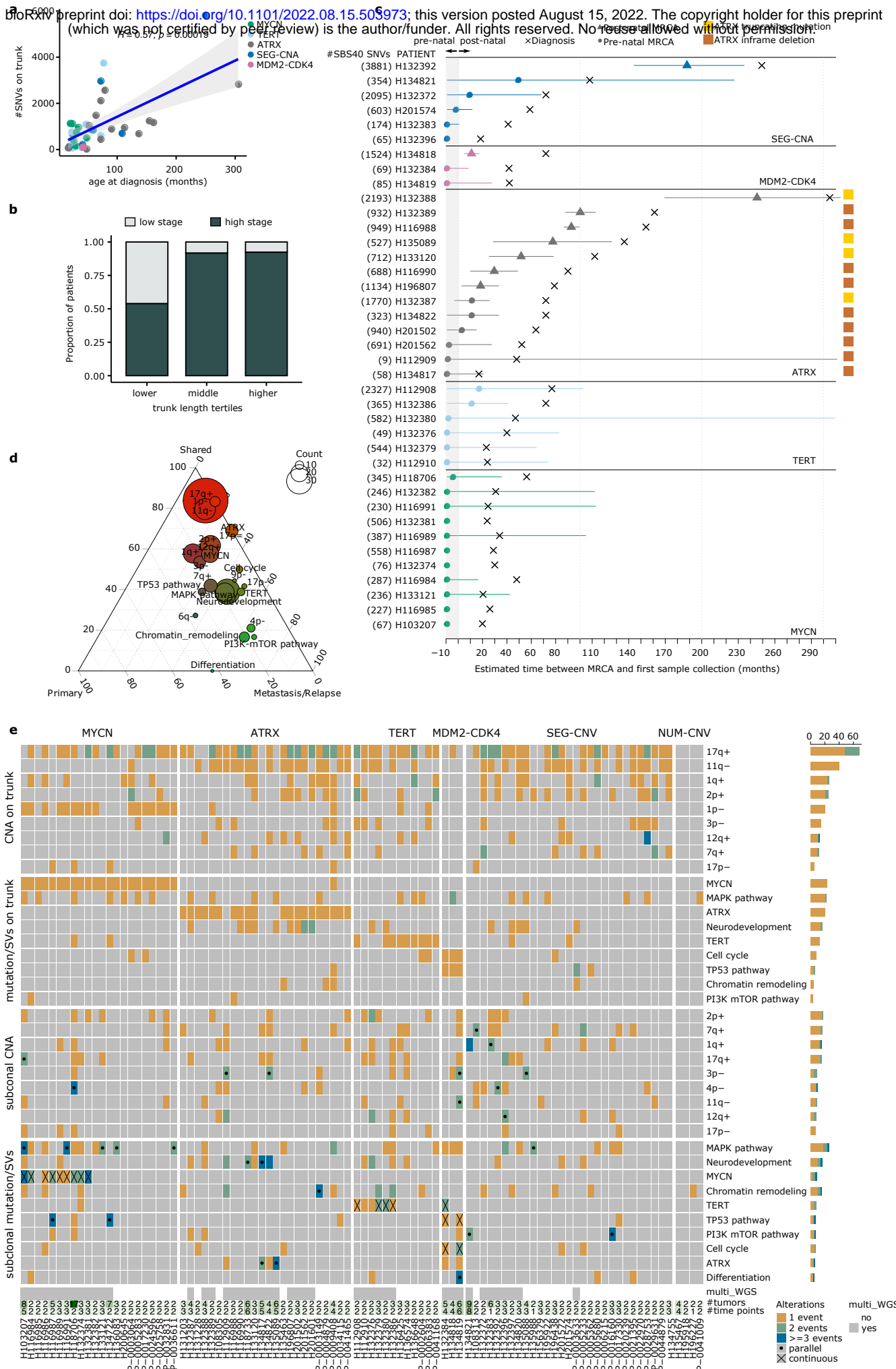


Figure 3

bioRxiv preprint doi: <https://doi.org/10.1101/2022.08.15.503973>; this version posted August 15, 2022. The copyright holder for this preprint (which was not certified by peer review) is the author/funder. All rights reserved. No reuse allowed without permission.

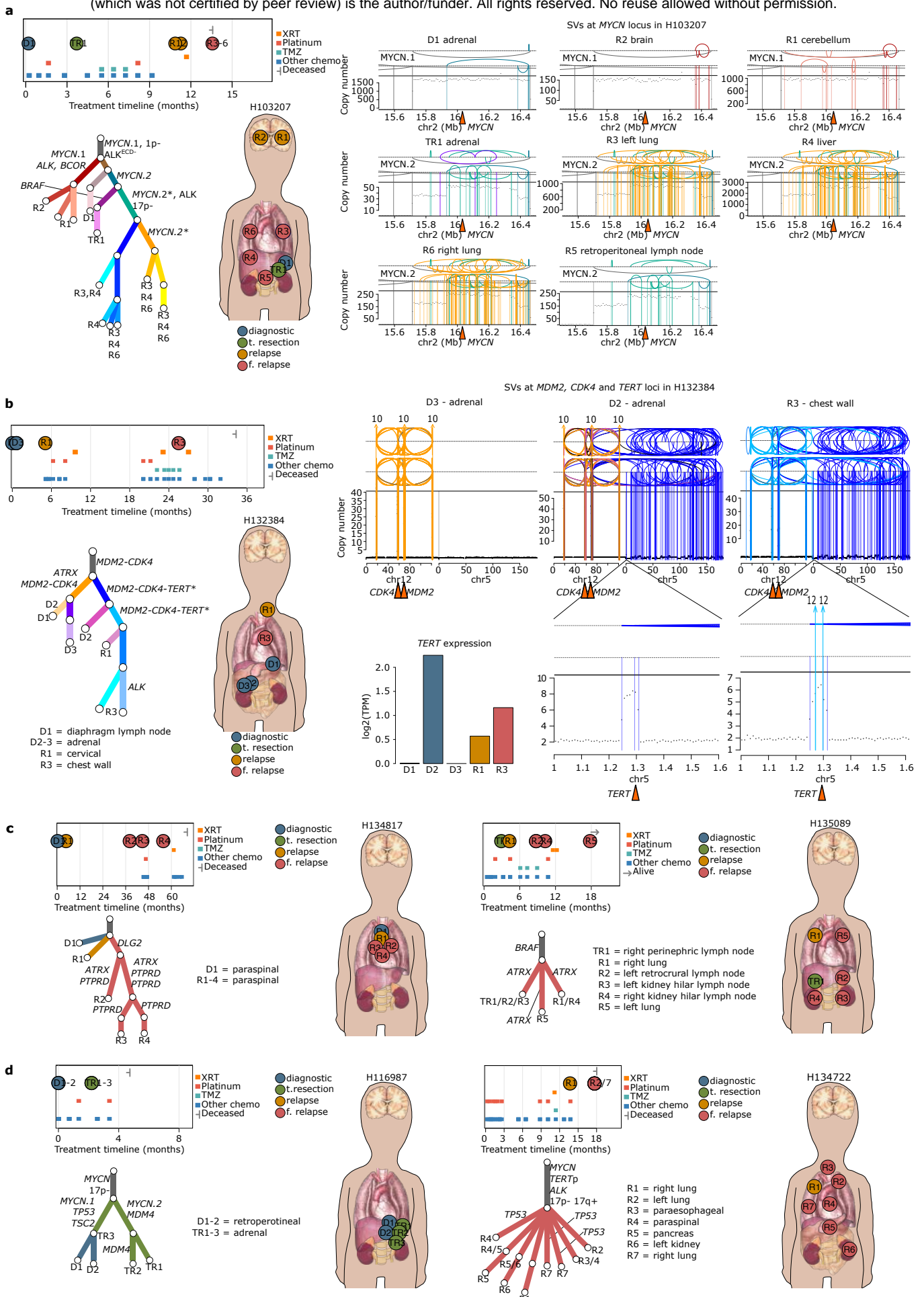


Figure 4. Preprint doi: <https://doi.org/10.1101/2022.08.15.503973>; this version posted August 15, 2022. The copyright holder for this preprint (which was not certified by peer review) is the author/funder. All rights reserved. No reuse allowed without permission.

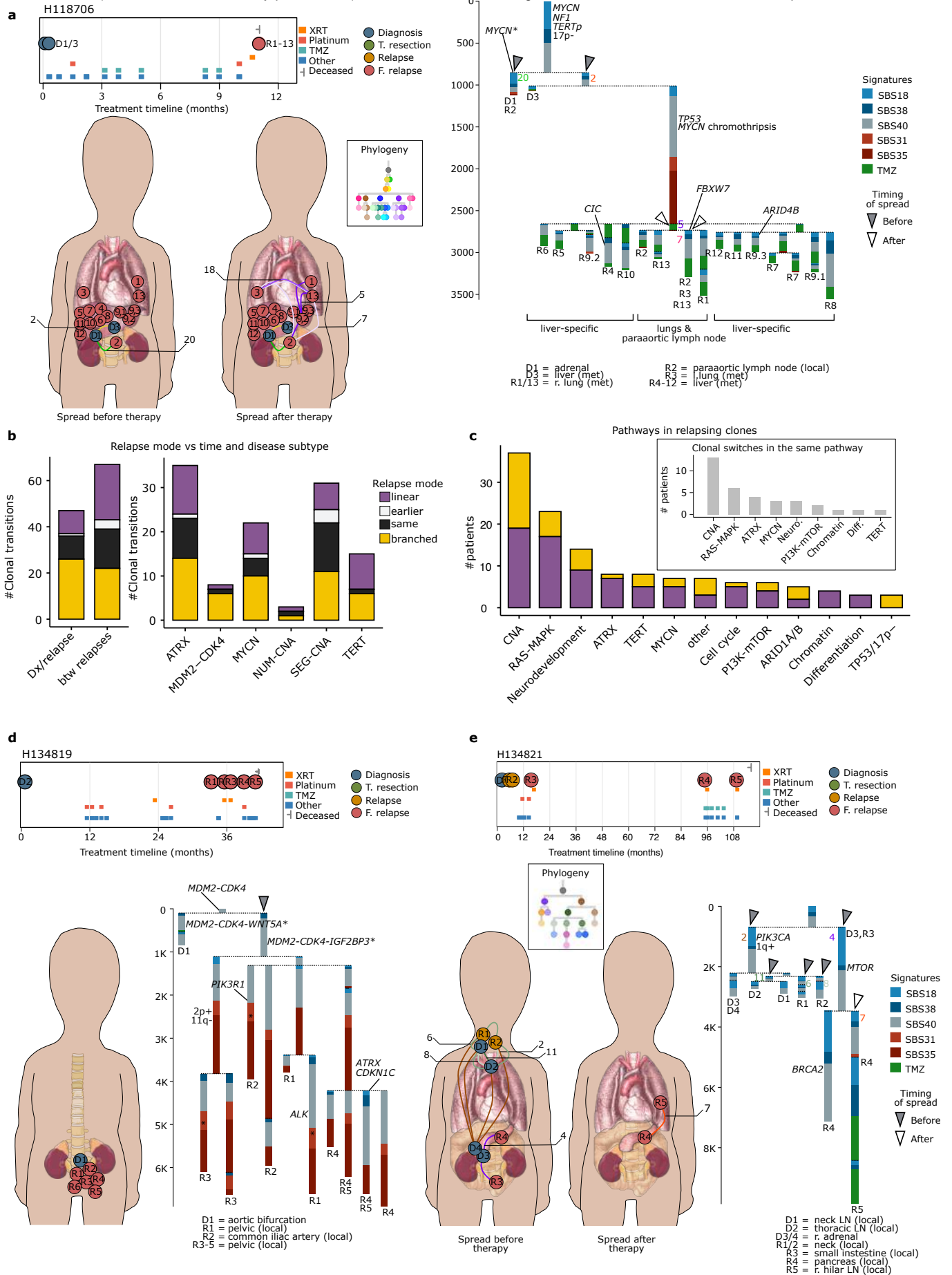
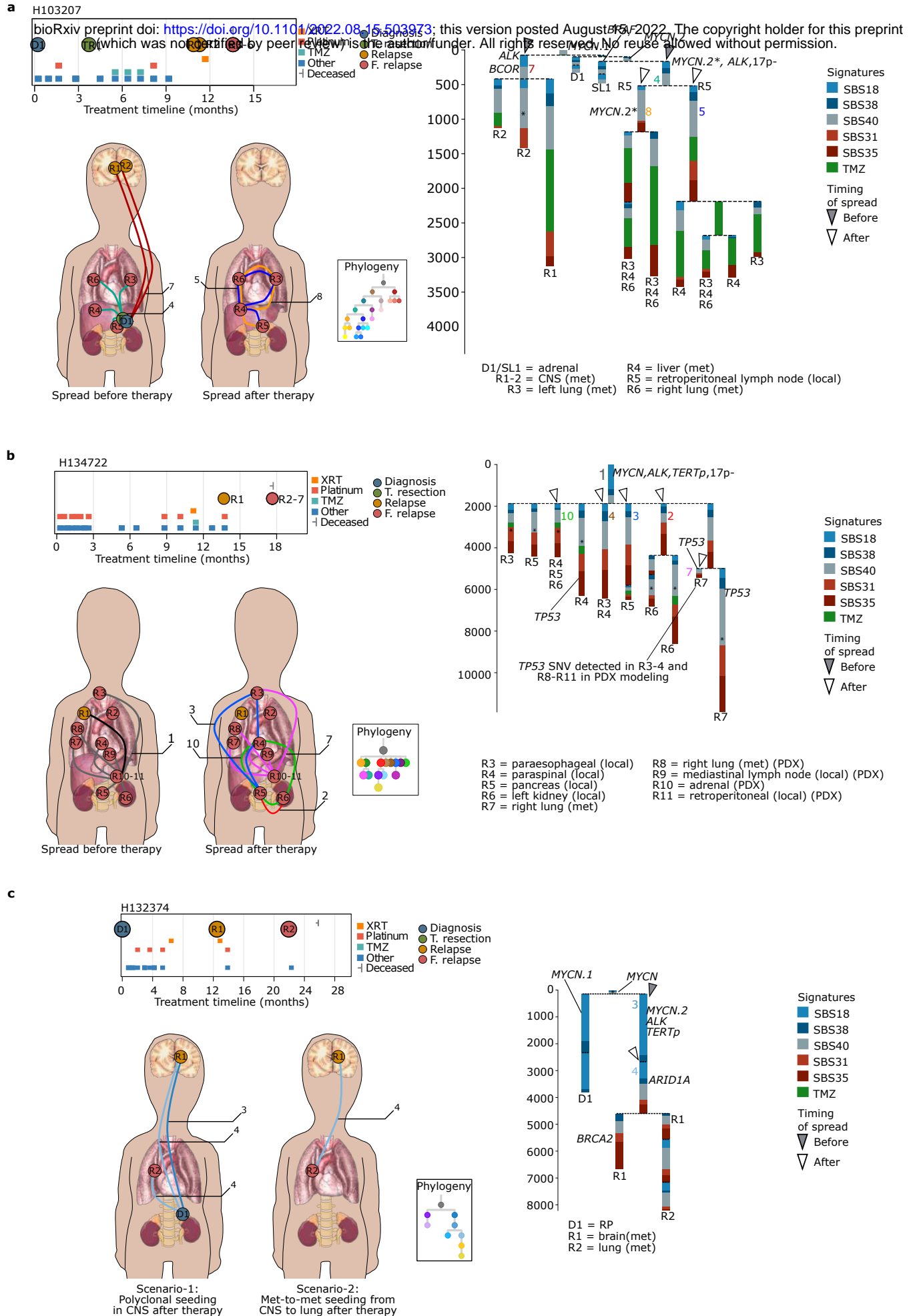
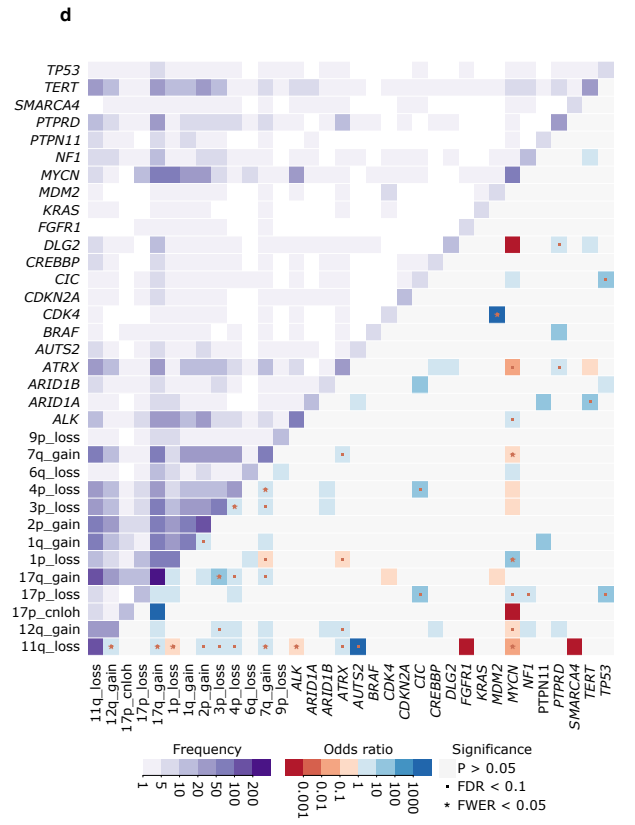
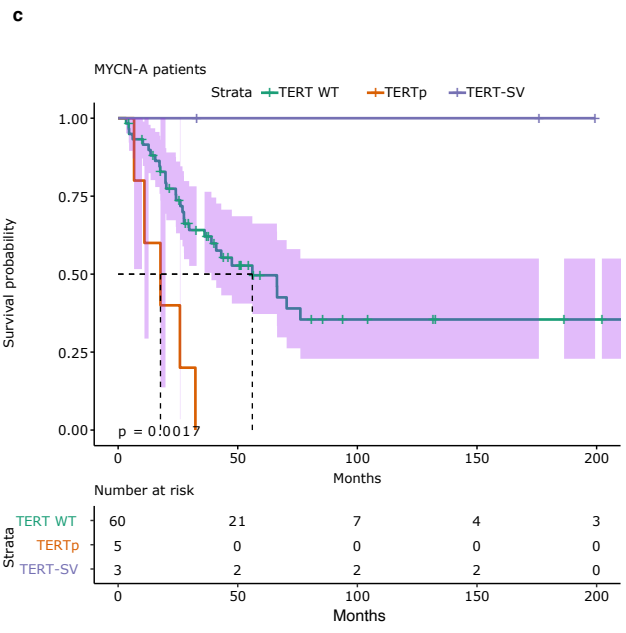
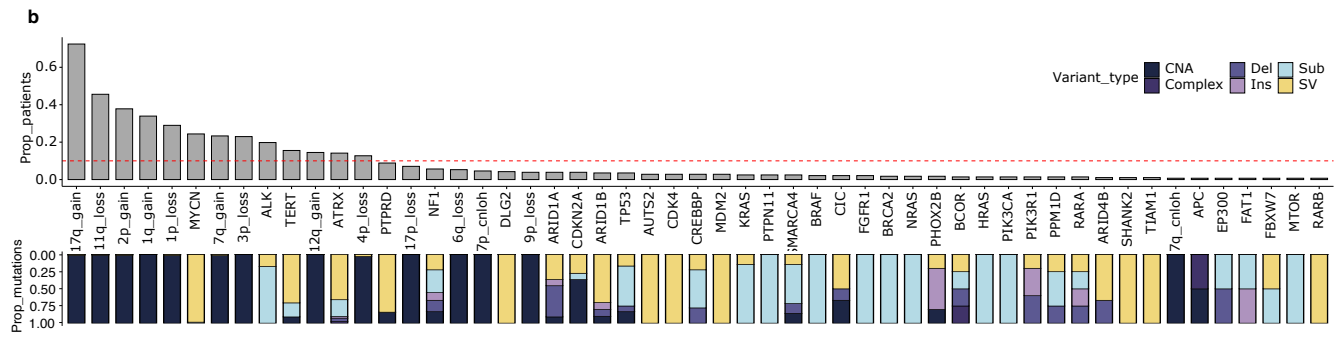
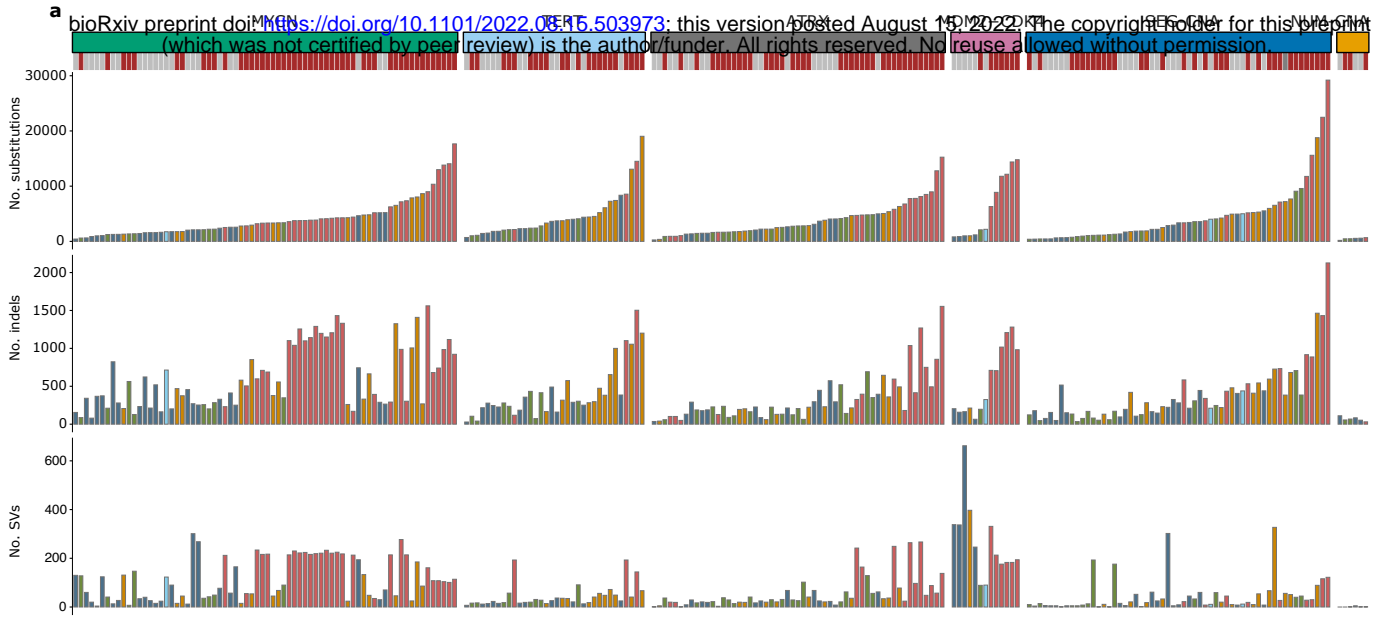


Figure 5



Extended Data Figure 1

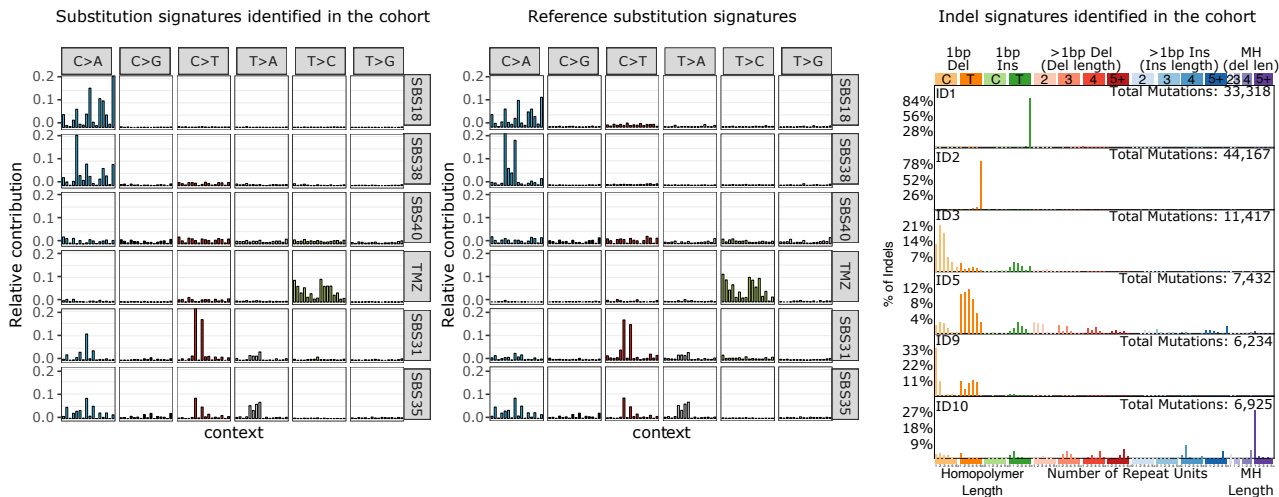
bioRxiv preprint doi: <https://doi.org/10.1101/2022.08.15.503973>; this version posted August 15, 2022. The copyright holder for this preprint (which was not certified by peer review) is the author/funder. All rights reserved. No reuse allowed without permission.



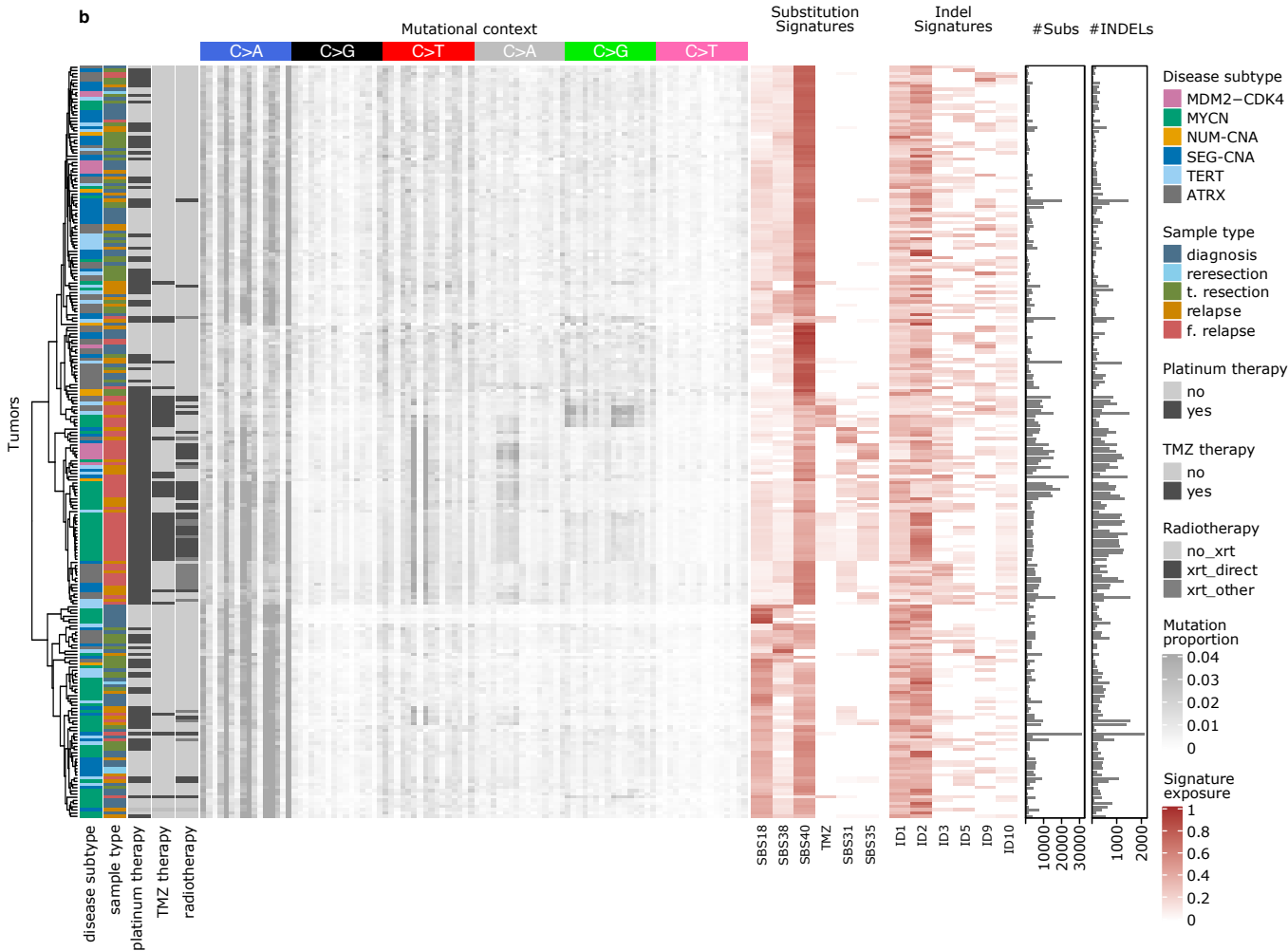
Extended Data Figure 2

bioRxiv preprint doi: <https://doi.org/10.1101/2022.08.15.503973>; this version posted August 15, 2022. The copyright holder for this preprint (which was not certified by peer review) is the author/funder. All rights reserved. No reuse allowed without permission.

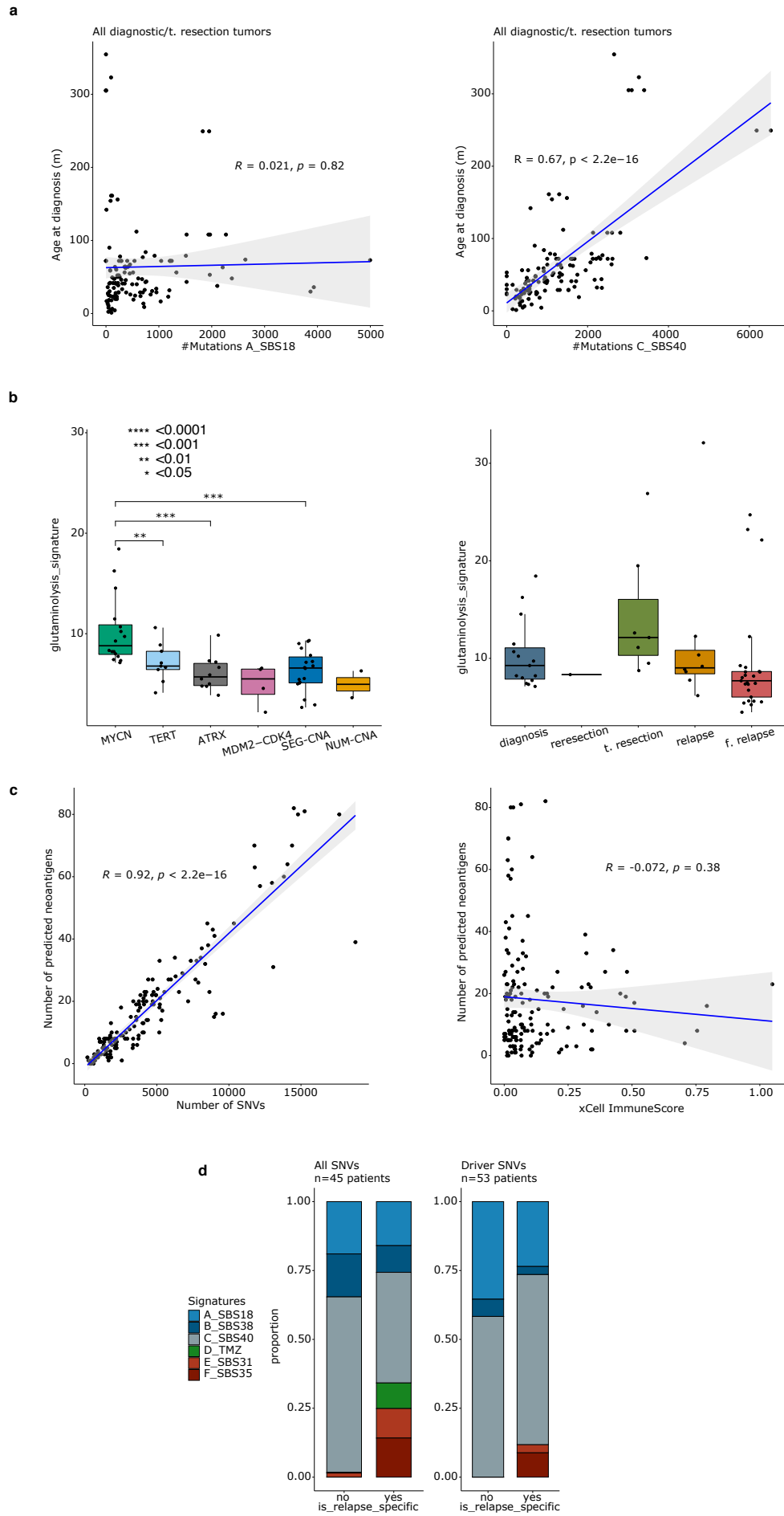
a



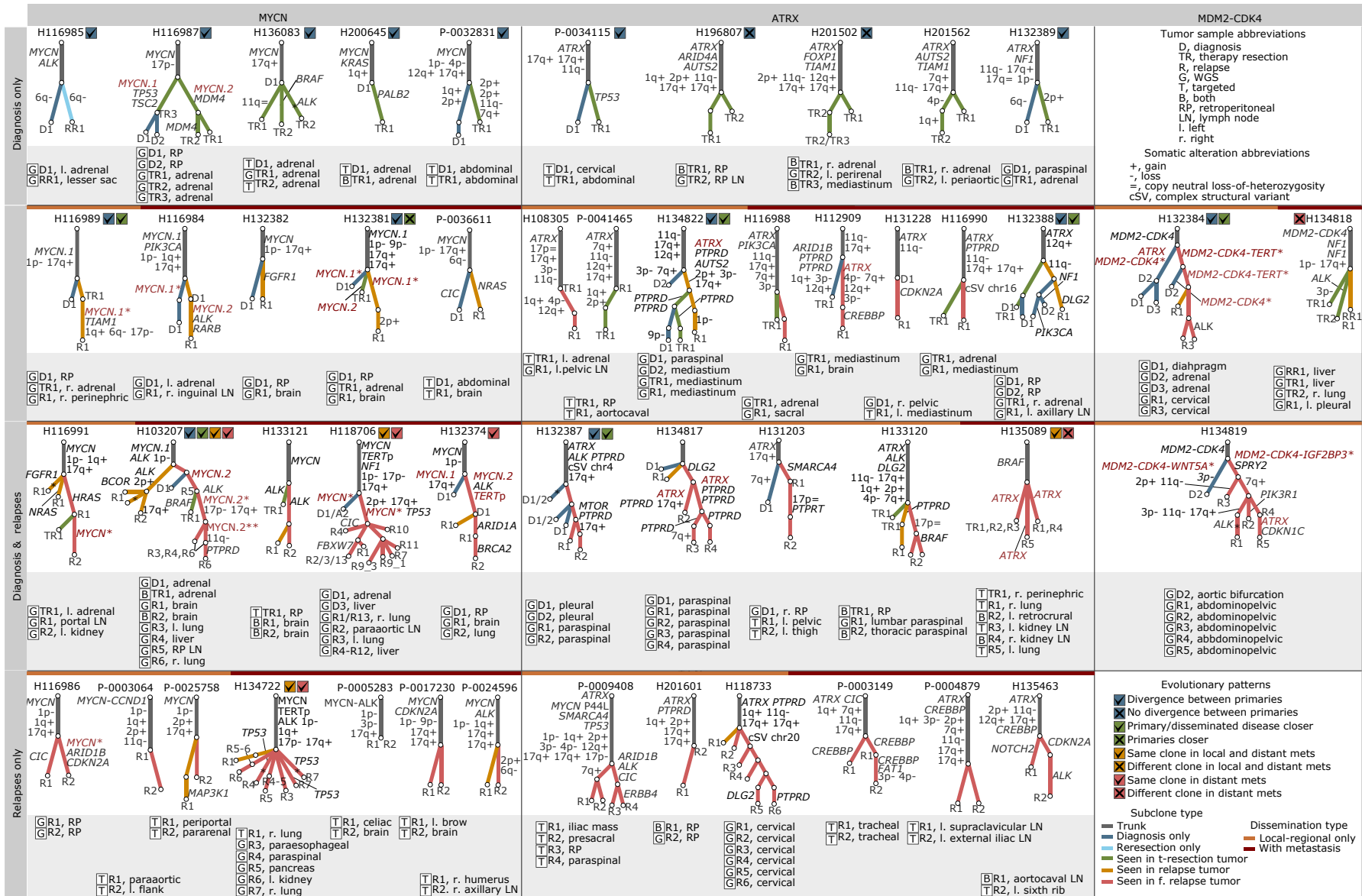
b



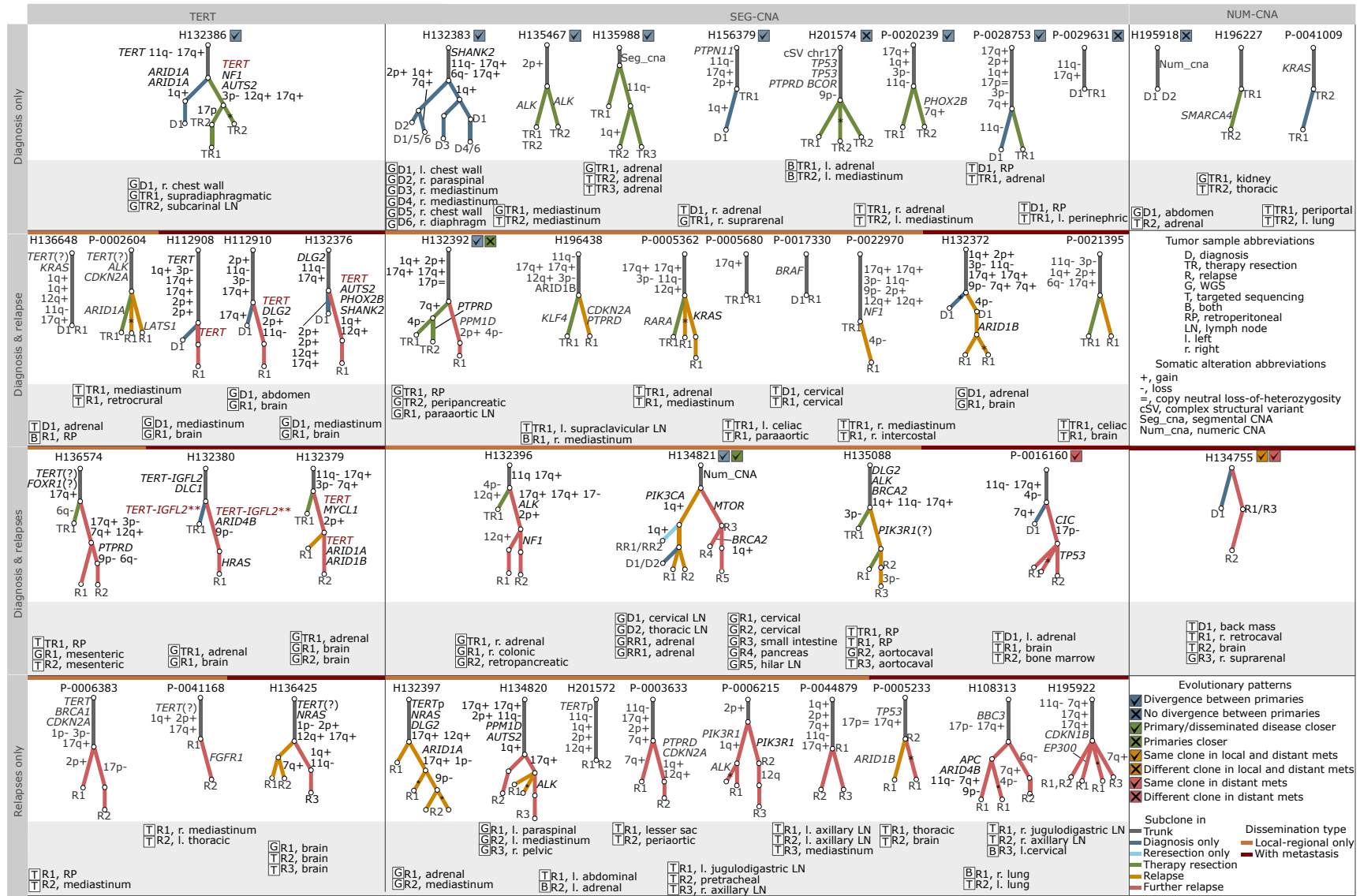
Extended Data Figure 3



Extended Data Figure 4



Extended Data Figure 5



Extended Data Figure 6

